



## Easy formation of functional liposomes in water using a pH- responsive microbial glycolipid: encapsulation of magnetic and up-converting nanoparticles

Lisa Van renterghem, Fabrizio Guzzetta, Patrick Le griel, Mohamed Selmane, Ghazi Ben Messaoud, Tabitha Tan su teng, Sierin Lim, Wim Soetaert, Sophie Roelants, Beatriz Julian-Lopez, et al.

### ► To cite this version:

Lisa Van renterghem, Fabrizio Guzzetta, Patrick Le griel, Mohamed Selmane, Ghazi Ben Messaoud, et al.. Easy formation of functional liposomes in water using a pH- responsive microbial glycolipid: encapsulation of magnetic and up-converting nanoparticles. ChemNanoMat, 2019, 5 (9), pp.1188-1201. 10.1002/cnma.201900318 . hal-02188401

**HAL Id: hal-02188401**

**<https://hal.science/hal-02188401>**

Submitted on 19 Jul 2019

**HAL** is a multi-disciplinary open access archive for the deposit and dissemination of scientific research documents, whether they are published or not. The documents may come from teaching and research institutions in France or abroad, or from public or private research centers.

L'archive ouverte pluridisciplinaire **HAL**, est destinée au dépôt et à la diffusion de documents scientifiques de niveau recherche, publiés ou non, émanant des établissements d'enseignement et de recherche français ou étrangers, des laboratoires publics ou privés.

# Easy formation of functional liposomes in water using a pH-responsive microbial glycolipid: encapsulation of magnetic and up-converting nanoparticles

Dr. Lisa Van Renterghem,<sup>a</sup> Dr. Fabrizio Guzzetta,<sup>b</sup> Patrick Le Griel,<sup>c</sup> Mohamed Selmane,<sup>c</sup> Dr. Ghazi Ben Messaoud,<sup>c</sup> Tabitha Tan Su Teng,<sup>d</sup> Prof. Sierin Lim,<sup>d</sup> Prof. Wim Soetaert,<sup>a,e</sup> Dr. Sophie Roelants,<sup>a,e</sup> Dr. Beatriz Julián-López,<sup>b</sup> Dr. Niki Baccile<sup>c,\*</sup>

a - InBio – Center for Industrial Biotechnology and Biocatalysis, Department of Biotechnology Faculty of Bioscience Engineering, Ghent University

b - Institute of Advanced Materials (INAM), Universitat Jaume I, Avda. Sos Baynat s/n, 12071 Castellón, Spain

c - Sorbonne Universités, CNRS, Collège de France, Chimie de la Matière Condensée de Paris UMR 7574, 4, Place Jussieu, 75005 Paris, France

d - School of Chemical and Biomedical Engineering, Nanyang Technological University, 70 Nanyang Dr., Singapore 637457, Singapore

e - Bio Base Europe Pilot Plant, Rodenhuiszekaai 1, 9042 Gent, Belgium

Corresponding author: niki.baccile@upmc.fr

## Abstract

The compartmentalization of colloids into topologically closed, vesicular, microphases offers an attractive mean to concentrate a functional cargo in aqueous solutions for a range of biomedical, cosmetic, and biotechnological applications. In this paper, we develop a simple, phospholipid-free, phase change method employing a pH-responsive glycolipid. The method is applied to the encapsulation of a sonicated, metastable, aqueous dispersion of functional colloids in the lumen of lipid vesicles: uncoated magnetic maghemite  $\gamma\text{-Fe}_2\text{O}_3$  and oleic-acid coated upconverting  $\text{NaYF}_4\text{:Yb/Ln}$  (Ln= Er or Tm) nanoparticles (NPs). We find a stable liposomal dispersion containing a sub-population of crowded liposomes with high concentrations of NPs. The encapsulated NPs, formed at nearly neutral pH and room temperature, are stable over time and towards extrusion. The vesicular microphase is entirely composed of pH-responsive glycolipids, which undergo a pH-mediated mesoscopic structural transition from an open lamellar ( $2 < \text{pH} < 4$ ) to topologically closed vesicular state ( $\text{pH} > 4$ ).

We also show that encapsulation successfully works with a stable colloidal aqueous dispersion of iron clusters stabilized in ferritin cages. This compartmentalization approach combining self-assembly with an orthogonal nonequilibrium dispersion of nanoparticles shows untapped potential for synthesizing unusual classes of mixed matter.

## Introduction

Encapsulation of nanoparticles into topologically-closed liposomes represents one of the most valuable advances for therapeutics purposes, because it enables an integration of the properties (e.g., optical, magnetic, and luminescent) of nanoparticles (NPs) with those of liposomes (protection, stability, biocompatibility).<sup>1</sup> Since the early 80s, nanoparticle-loaded liposomes have been explored to probe cell-liposome interactions on gold<sup>2</sup> and magnetite.<sup>3,4</sup> More recently, there has been more focus on the diversity of not only the nature of the encapsulated NPs, like silica and quantum dots,<sup>5</sup> but also to achieve better encapsulation methods.<sup>6</sup> The latter allows, for instance, high NPs load uptakes by the liposomes<sup>7</sup> or the development of stimuli-responsive vectors based on lipids<sup>8,9</sup> or polymers.<sup>10,11,12</sup> In the last decade, liposomal encapsulation of iron-loaded ferritin cages has even been associated with the fundamental questions underlying the origins of life.<sup>13</sup>

The case of magnetoliposomes, an idea being at least three decades old,<sup>3,4,14</sup> is particularly interesting. Magnetoliposomes refer to liposomes that contain magnetic NPs (mainly  $\text{Fe}_3\text{O}_4$  and  $\gamma\text{-Fe}_2\text{O}_3$ ) in their lumen, lipid bilayer or at the vesicle surface,<sup>1,9,15</sup> and which are particularly interesting for the well-known applications in hyperthermia or as contrast agent in magnetic resonance imaging.<sup>16</sup> Either alone or in combination with drug loading, liposomal protection increases the blood circulating time, bioavailability and delivery.<sup>1,8,9</sup> The first reported preparation approach to insert NPs into the liposome lumen employed a classical precipitation method:<sup>4</sup> simple mixing of pre-formed DMPG<sup>17</sup> and DPPG<sup>18</sup> phospholipid liposomes with lauric acid coated  $\text{Fe}_3\text{O}_4$  particles was shown to precipitate NP-loaded vesicles. Other methods have been employed, such as reverse phase evaporation,<sup>14,19,20,21</sup> or *in-situ* liposomal precipitation of the NPs.<sup>6</sup> Thin film hydration, double emulsion methods, or ethanolic injection can also be used.<sup>13,21,22,23</sup> Recent review papers address the synthesis of magnetoliposomes more extensively.<sup>1,9,16</sup> Similar encapsulation strategies are employed for other materials such as metal,<sup>24</sup> oxides<sup>5</sup> or luminescent nanoparticles including quantum dots<sup>5</sup> and upconverting lanthanide-doped fluorides.<sup>25</sup>

Although these methods are valuable, some of them use toxic halogenated solvents (e.g., chloroform), require elaborate methodologies (e.g., evaporation under vacuum) and in general

the use of stable colloids. The latter is an important point. Most, if not all, of these methods require the use of stable colloids in general. In most cases, many nanoparticle systems are passivated by a hydrophobic layer,<sup>25</sup> which easily guarantees encapsulation in the vesicle bilayers.<sup>9,15,16</sup> However, ligand exchange, commonly regarded as a tedious unavoidable step, use of surfactants or hydrophilic coatings, become then necessary for encapsulation in the lumen in water-based media.<sup>16,21</sup> Moreover, the interaction between the (coated or uncoated) NPs with the phosphate groups of phospholipids may destabilize the bilayer membrane, thereby affecting the vesicle formation mechanism and reducing their stability.<sup>1,9</sup> It is then interesting to develop an encapsulation water-based method applicable to a broad range of colloids out of thermal equilibrium. Non-equilibrium encapsulation is generally obtained in food and material science through dynamic processes such as spray drying,<sup>26,27</sup> while recent theoretical work could explore its possibilities in the compartmentalization within elastic geometries like carboxysomes.<sup>28</sup>

Lipid switches<sup>29,30</sup> were recently combined with classical phospholipid liposomes to deliver a cargo upon application of an external stimulus (pH, ion). In this paper, we take inspiration of this concept to develop a fully water-based (at nearly neutral pH) bulk phase-change method to encapsulate, rather than release, a cargo composed of metastable colloids into vesicles. The latter are compartments entirely free of phospholipids and only composed of pH-responsive lipid switches. Vesicle formation is dynamic, reversible, rapid and entirely controlled through pH. We apply this method to the formation of magnetoliposomes, chosen as model system abundantly described in the literature,<sup>4,9</sup> from an unstable dispersion of bare (uncoated) maghemite  $\gamma\text{-Fe}_2\text{O}_3$  nanoparticle aggregates. We then extend it to the encapsulation of hydrophobic, oleic acid coated,  $\text{NaYF}_4\text{:Yb/Ln}$  (Ln= Er or Tm) upconverting nanocrystals.<sup>31</sup> Both systems, otherwise sedimenting/segregating in/from water, are driven out of equilibrium by applying strong sonication before encapsulation through a pH-jump process.

The method proposed here involves a lamellar-to-vesicle phase transition, conceptually analogous to the mechanism occurring in thin film hydration or in the preparation of vesosomes,<sup>32</sup> but driven by a simple pH jump (generally  $\sim 4$  to  $\sim 6$ ) in bulk water. Instead of common complex formulations combining phospholipids with pH-responsive lipids<sup>8,33,34</sup> or block-copolymers,<sup>35</sup> we use a single pH-sensitive microbial glycolipid (GL) (Figure 1).<sup>36</sup> Microbial glycolipids are biobased compounds known for their stimuli-responsive properties,<sup>37,38,39</sup> their biodegradability and low toxicity,<sup>40-45</sup> and for these reasons particularly interesting for biomedical applications. GL are known to form a set of closed vesicular microphase via a simple pH-jump below  $\leq 6.2$  and a lamellar precipitate below pH  $\sim 4$ .<sup>46</sup>

Using a combination of cryo-TEM, light and X-ray scattering, we find that high loads of nanoparticles tend to occupy a limited number of vesicular compartments. This feature is also observed upon loading of ferritin nanocages,<sup>47</sup> a result which agrees with the finding of Luisi et al.,<sup>13</sup> who proposed that the massive occupation of a small fraction of vesicles, coexisting with a large majority of empty vesicles, could explain the compartmentalization of heregenous genomic material in the early stages of life formation.

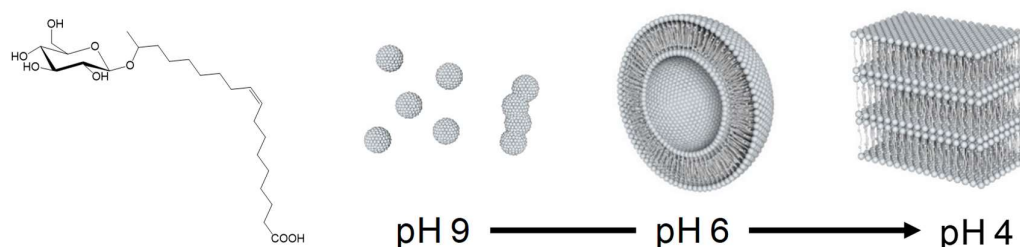


**Figure 1 - Acidic form of the microbial glucolipid GC18:1 (GL) and its corresponding pH-dependent phase behaviour at room temperature: micelles, vesicle, lamellar.**

## Material and Methods

**Synthesis of glycolipid GC18:1 (GL).** GLs were produced in a scaled-up bioreactor experiment (100 L) by the *S. bombicola* strain *ΔugtB1* described by Saerens et al.<sup>36</sup> The detailed production, purification and hydrolysis process to obtain the compound in Figure 1 has been reported elsewhere.<sup>46</sup> GLs contain about 90 % and 7 % of the subterminal (glycosidic bond between glucose and the C17 of the fatty acid chain, Figure 1) and terminal (glycosidic bond between glucose and the C18 of the fatty acid chain) congener, respectively. The remaining 3 % is constituted by di-unsaturated C18:2 and saturated C18:0 impurities.

**Preparation of iron oxide nanoparticles (NPs).** Iron oxide NPs were synthesized using the co-precipitation method by adapting the standard protocol<sup>48,49</sup> to obtain the inverse spinel structure typically observed in magnetite, where  $[\text{Fe}^{2+}]/[\text{Fe}^{3+}] = 0.5$ . Specifically, 0.177 g of  $\text{FeCl}_3 \cdot 6\text{H}_2\text{O}$  was mixed with 0.108 g of  $\text{FeCl}_2 \cdot 4\text{H}_2\text{O}$  in a round-bottom flask containing 20 mL of Milli-Q water. To this solution, 2.7 mL of a 28 % ammonium hydroxide solution was gradually added under continuous mechanical stirring. The system was maintained in an argon-rich environment to limit oxidation. The resulting black precipitate was extracted by magnetically-assisted sedimentation and washed with MilliQ water. This operation was repeated three times to remove any residual salts.

**Preparation of upconverting nanoparticles (UCNP).** Upconverting oleic acid capped  $\text{NaYF}_4:\text{Yb/Er}$  and  $\text{NaYF}_4:\text{Yb/Tm}$  nanoparticles (20%-Yb and 0.5%-Ln, Ln= Er, Tm) molar

ratio replacing yttrium ions in the lattice, labelled as UCNPs) of size between 20 nm and 40 nm were prepared according to ref. 50.

**Iron-loaded ferritin cages preparations and characterization.** The iron-loaded ferritin cages (AfFtn) are prepared as previously described.<sup>47,51</sup> Briefly, the ferritin is derived from the archaeon *Archaeoglobus fulgidus* and was produced recombinantly in *E. coli* strain BL21(DE3)CodonPlus-RIL (Stratagene) with IPTG induction. The harvested cells were sonicated and heat-treated at 85°C for 10 minutes. The insoluble fraction and denatured proteins were removed using ultracentrifugation and the supernatant was passed through 0.22 µm filter. No further purification was performed for this report. Iron was loaded by adding Fe<sub>2</sub>SO<sub>4</sub> dropwise until 4800 Fe/cage had been loaded. To remove the unloaded iron, the sample was desalted, concentrated using 100 kDA MWCO Amicon filter, and sterile filtered using 0.22 µm syringe filter. The iron-loaded ferritin (Fe4800)AfFtn preparation was characterized by dynamic light scattering (DLS) technique to confirm that the hydrodynamic size was ~13 nm and the protein concentration was estimated using Bradford assay.<sup>47,51</sup>

**NPs-containing vesicle preparation.** Ten mL of the NPs solution were set to pH 9 and bath-sonicated during 30 min to one hour. After sonication, the NPs solution was mixed at room temperature to 10 mL of a micellar GL solution (0.29 g GL in 10 mL) at pH 9. The NPs GL mixture at pH 9 (referred to NPs GL, pH9, sample S2) was kept under stirring for few minutes before use. *Note: the NPs solution is not sonicated in the presence of the GL solution.* According to the data in Baccile et al.,<sup>46</sup> GL self-assembles into vesicles at pH values below 6.2. Thus, to prepare vesicles, two aliquots of the NPs GL solution at pH 9 were acidified using 1 M HCl solution: in aliquot 1, the pH is lowered to 6, and this sample is referred to as NPs GL, pH6 (sample S3) and in aliquot 2, the pH is lowered below 4 and then increased again to pH 6 and named NPs GL, pH2→pH6 (sample S4). The latter will also be referred to as the *manual pH-jump approach 2*, where *approach 1* corresponds to sample S1, that is a control experiment only containing NPs and free of GL. In a second control experiment (sample S5), the pH of the NPs (GL-free) solution was lowered to 6 with 1 M NaOH, and 0.45 g of non-acetylated acidic sphorolipids were subsequently added, similarly to the two-step procedure described in Baccile et al.<sup>55</sup> Sphorolipids are microbial glycolipids having a disaccharide headgroup and known to self-assemble into micelles, instead of vesicles, under the acidic pH conditions.<sup>46</sup> The detailed sample compositions are given in Table 1.

**Table 1 – Composition table of the samples studied in this work.** GL: acidic glucolipid GC18:1 (Figure 1), NPs: γ-Fe<sub>2</sub>O<sub>3</sub> nanoparticles,<sup>55</sup> SL: sphorolipids.<sup>55</sup> The concentration of NPs mother solution is estimated by gravimetric analysis. Samples S2 through S5 are obtained by mixing 1:3 vol:vol of mother GL (40 mg/mL)

and NPs (4.2 mg/mL) solutions, both at pH 9.  $pH_i$ ,  $pH_m$  and  $pH_f$  respectively indicate the initial, middle and final pH. If no pH change has occurred,  $pH_i = pH_f$ . All pH variations are performed by hand using 1 M HCl and 1 M NaOH solutions.

Sample name	Sample code	$C_{GL}$ / mg/mL	$C_{SL}$ / mg/mL	$C_{NPs}$ / mg/mL	$pH_i$	$pH_m$	$pH_f$
GL	-	10	-	-	9	-	6
NPs	S1	-	-	4.2	9	-	9
NPs GL pH 9	S2	10	-	3.2	9	-	9
NPs GL pH 6	S3	10	-	3.2	9	-	6
NPs GL pH 2 $\rightarrow$ pH 6	S4	10	-	3.2	9	2	6
NPs SL pH 6	S5	-	10	3.2	9	-	6

The *manual pH-jump (approach 2)* described above has been performed manually and for this reason we have tested a series of additional methods to evaluate the robustness of the encapsulation process and to control the vesicle size distribution. These experiments have been performed on both a NPs-free solution constituted of vesicles only (GL in Table 1) and a mixed NP and GL (sample S4 in Table 1). *Extrusion (approach 3)*: after the *manual pH-jump (approach 2)* the solution is extruded (10 cycles) at 1 mL/min through a 0.45  $\mu$ m filter. Extrusion is commonly used to control vesicle size in the hundred nanometer range.<sup>52,53,54</sup> *Sonication (approach 4)*: after the *manual pH-jump (approach 2)*, the solution is sonicated for 20 s using an immersive ultrasound probe. Sonication is commonly used to prepare vesicle of diameter below 100 nm.<sup>52</sup> *Controlled pH-jump (approach 5)*: after the pH is lowered to 2, pH is increased to 6 using a 1 M NaOH solution injected at 0.5  $\mu$ L/min under stirring. *Dialysis pH-jump (approach 6)*: after the pH is lowered to 2, pH is increased to 6 by dialyzing the solution against a water reservoir at pH 6 using a 3500 MWCO (Spectra/Por®) membrane. Finally, to guarantee homogeneous dispersion of the vesicles and NPs, solution are kept under stirring during the *manual pH-jump* and *controlled pH-jump* processes.

**Preparation of iron-loaded ferritin-containing vesicles.** The procedure was adapted from the NPs-containing vesicle process. The stock (Fe4800)AfFtn solution (0.88 mg/mL, pH 7.4) was mixed with the a micellar GL solution (40 mg/mL, pH 7.4) to achieve respective final concentrations of 0.66 mg/mL and 10 mg/mL. The pH was then lowered to about 3.9 (using  $\sim$  6  $\mu$ L HCl 5 M) to avoid (Fe4800)AfFtn aggregation. The pH is then increased to 6 using three selected approaches described above. *Manual pH jump (approach 2)*: pH is manually increased by manual addition of 1 M NaOH solution. *Controlled pH-jump (approach 5)*: a 1 M NaOH solution is injected at 0.5  $\mu$ L/min under stirring until pH 6 was achieved. *Extrusion (approach 3)*: the (manual) pH jump solution is extruded (10 cycles) at 1 mL/min through a 0.45  $\mu$ m filter.

Note: (Fe4800)AfFtn is water-dispersible, therefore it is never sonicated.

**Preparation of UCNP-containing vesicles.** To a 10 mg/mL micellar GL solution in water at pH 9, we add the dried oleic-acid-capped NaYF<sub>4</sub>:Yb/Er and NaYF<sub>4</sub>:Yb/Tm UCNP powder at concentration of 5 mg/mL. The UCNP sample is water-insoluble and for this reason sonication is necessary to help dispersion. For the encapsulation, we employ *the manual pH jump (approach 2)*: pH is reduced to 4 (manual dropwise addition of  $\mu$ L amounts of 0.5 M HCl) and then increased to ~6 (manual dropwise addition of  $\mu$ L amounts of 1 M NaOH). The same protocol applies to a control solution only containing the UCNP sample, without adding GL. Despite the hydrophobic character of the oleic acid-coated UCNP, sonication is enough to disperse them in water, although sedimentation is fast for the control, GL-free, experiment.

**Sedimentation experiments using photoluminescence spectroscopy.** *Free sedimentation*: the UCNP dispersion is placed in a quartz cuvette and irradiated with a CW laser source ( $\lambda$ = 980 nm) at a power density of 105 W/cm<sup>2</sup>. Emission spectra were recorded after 0, 10, 20, 30, 60, 120, 300, 600, 1200, 1800, 3600, 5400 s. *Forced sedimentation*: The setup and conditions for photoluminescence measurements were identical to the free sedimentation. However, the encapsulated UCNP dispersion was centrifuged at 2000 rpm in a time scale comprised between 0 and 300 seconds, and emission spectra were taken after 10, 20, 30, 60, 120 and 300 seconds of centrifugation.

**Light scattering (LS) experiments.** Light scattering experiments were performed on a Malvern Zetasizer Nano ZS instrument ( $\lambda$ = 633 nm) at constant shutter opening and same sample-to-detector distance. The diffused light was expressed in terms of the derived count rate in kilocounts-per-seconds (kcps). All solutions were diluted 100 times prior to analysis. Two measurements were performed, the first one on the solution itself and the second one on the supernatant of the same solution, after magnetically-assisted sedimentation of the suspended NPs using a neodymium magnet.

**Transmission Electron Microscopy (TEM).** TEM was performed on a FEI Tecnai 120 Twin microscope operating at 120 kV and equipped with a high resolution Gatan Orius CCD 4k x 4k numeric camera. DigitalMicrograph™ software was used for image acquisition. TEM images acquired in cryogenic mode were obtained from the same instrument. The sample holder was a Gatan Cryoholder (Gatan 626DH, Gatan). DigitalMicrograph™ software was used for image acquisition. Cryo-fixation was done on a homemade device. The solutions were deposited on glow discharged holey carbon coated TEM copper grids (Quantifoil R2/2, Germany). Excess solution was removed and the grid was immediately plunged into liquid ethane at -180°C. All grids were kept at liquid nitrogen temperature throughout all



experimentation.

**Small Angle X-ray Scattering (SAXS).** SAXS experiments were recorded at the high brilliance ID02 beamline at the ESRF synchrotron (Grenoble, France) using a 1 m detector-to-sample distance and a flow-through polycarbonate capillary. Acquisition time was 1 s per pH value. pH was changed in-situ in the experimental hutch and followed live. More details on the experimental setup have been provided in Baccile et al.<sup>46</sup> Data were acquired using a CCD camera and integrated azimuthally to obtain a typical  $I(q)$  spectrum. Contribution of the solvent (water at pH 11.6) and capillary were measured prior to the experiment and accordingly subtracted during the data treatment. All data were corrected for the transmission of the direct beam.

Additional SAXS experiments were performed on a laboratory three-pinhole type S-MAX 3000 RIGAKU Nanoviewer instrument using a monochromatic Cu-K $\alpha$  radiation produced by a microfocus (20 microns x 20 microns) sealed tube X-ray source (MicroMax 002+ RIGAKU working at 40 W) and equipped with a two-dimensional multi-wire proportional gas detector. The sample-to-detector distance was set to 1469 mm. The applied voltage and filament current were 40 kV and 50 mA respectively. The  $q$ -range calibration was made using a silver behenate standard sample ( $d_{\text{ref}} = 58.38 \text{ \AA}$ ). The measured intensity was always divided by the sample transmission and appropriate masking was done to eliminate the beam-stop shadow contribution and imperfection of the 2D detector. Quartz sample holders of 1 mm diameter were used in a flow-through mode using a home-made device, thus assuring that the background signal was constant for all samples. The subtracted background was constituted by the water-containing quartz capillary. The acquisition time per sample is 1 h.

**X-ray Diffraction (XRD).** XRD data were recorded on the dried powders using a Bragg-Brentano  $\theta$ -2 $\theta$  ( $\lambda = 1.54 \text{ \AA}$ ) goniometer Bruker D8 Discover instrument.

**Differential thermal analysis (DTA).** DTA was performed in a Mettler-Toledo TGA/SDTA851e/LF/1600 instrument. The analysis of the powders was carried out in Pt crucibles at a heating rate of 5 °C/min under air atmosphere over the range of 20-900 °C and using alumina as reference.

**Photoluminescence spectroscopy.** Upconversion photoluminescence was recorded using an infrared laser diode RLTM DL-980-2W module (980 nm  $\pm$  5 nm, 2 W cw) from Roithner LaserTechnik, and a Black Comet CXR (StellarNet) optical fiber as detector. The emission was measured using dispersions of the UCNPs (10 mg in 1 mL of ethanol for bare nanoparticles, or in 1 mL of water for the samples encapsulated in glycolipids) and focusing the laser on the samples at a pump density of 105 W/cm<sup>2</sup>.

## Results and discussion

**Encapsulation of sonicated iron oxide nanoparticles.** The XRD of the bare iron oxide NPs is represented by the diffractogram N°1 on Figure 2, which shows the d-values: 2.967, 2.527, 2.092, 1.714, 1.614, 1.478 Å, corresponding, to the (220), (311), (400), (422), (511), (440) Bragg diffraction planes of the iron oxide spinel cubic structure (JCPDS file, N° 19-0629), respectively. This is attributed to a maghemite structure, previously identified using Mössbauer spectroscopy.<sup>55</sup> The typical size (below 10 nm) and aggregation state of this sample are shown by TEM in Figure S 1 (sample referred to as NPs).<sup>55</sup> The magnetic nature of the NPs (Figure 3) shows the attraction of the NP sample to the magnetic field of a neodymium magnet leaving the supernatant solution completely clear. The observation is also confirmed by the light scattering (LS) data in Figure 3 (sample S1) before (white bars, strong scattering) and after (grey bars, no scattering) exposure to the magnet. This is explained by the strong aggregation of the uncoated NPs (Figure S 1, NPs sample) in water. On the other hand, GL mainly assembles into micelles in water at pH 9, as shown by the characteristic SAXS scattering signal, shown in Figure 2b. The same compound is also known to form vesicles when the pH is lowered from 9 to 6, as previously demonstrated by us<sup>37,46</sup> and shown here by the typical SAXS scattering signal recorded at pH 6.07 in Figure 2b. The SAXS pattern is characterized by a broad oscillation at  $q$  above  $0.1 \text{ \AA}^{-1}$ , attributed to the form factor of a lipid bilayer, and an intense scattered intensity at  $q$  below  $0.05 \text{ \AA}^{-1}$ , the slope of which in log-log scale is close to -2, a typical value found for planar surfaces. A detailed analysis of the form factor through model-dependent fitting of SAXS data presented in Figure 2b can be found in ref. 37.

Addition of GLs to the bare nanoparticle solution at pH 9 does not modify the NPs crystal structure (XRD pattern N°2, Figure 2a), nor the overall aggregation state (sample NPs GL, pH9 in Figure S 1). However, upon exposure to the magnet most NPs are removed from the solution, but the latter still has a light brown colour, indicating a small dispersion of NPs in solution. This is confirmed by the slightly higher scattering signal in LS data (sample S2) in Figure 3. Given the strong molecular similarity between GLs and sophorolipids (SLs), GLs can certainly stabilize a small fraction of the iron oxide NPs by a simple adsorption at their surface via the carboxylate group, a phenomenon observed in a previous study.<sup>55</sup>

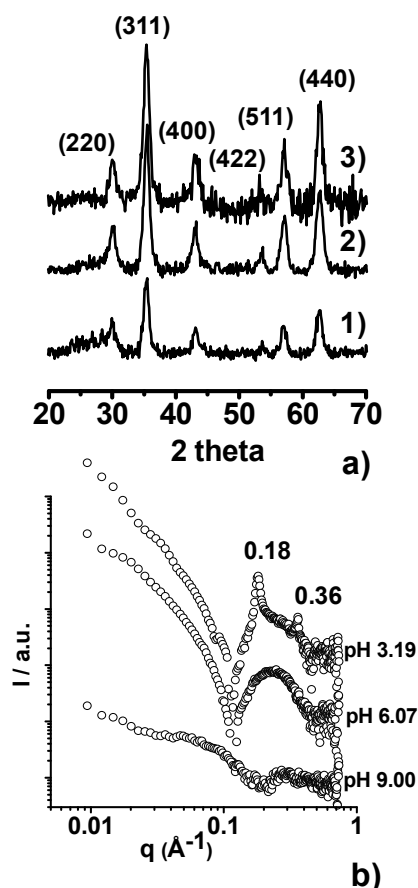


**Figure 2 – a) X-ray diffraction patterns of 1) iron oxide NPs, 2) NPs GL at pH 9 and 3) NPs GL at pH 6. Reported values relate to the Miller (hkl) indices of the Bragg diffraction planes. b) SAXS curves were recorded on the ID02 line of ESRF synchrotron for a pure GL solution at pH values between 3 and 9. The solutions at pH 6.07 and pH 3.19 have been directly obtained from the solution at pH 9.00 by adding 1 M HCl solution.**

When the pH of the NPs GL solution is lowered from 9 to 6, one can confirm that the nanoparticle crystal structure is intact (XRD pattern N° 3, Figure 2a). Upon approaching an external magnet to the vial, most NPs are attracted, thus leaving the solution slightly yellowish (Figure 3b, sample S3) due to the spurious presence of GL-coated NPs in solution. Light scattering of sample S3 (diluted, Figure 3a) qualitatively confirms the loss in the scattered intensity of the supernatant upon magnetically-assisted sedimentation. Nevertheless, Figure 3b shows that sample S3 (undiluted) supernatant is slightly turbid, if compared to samples S1 or S2; this is explained, and actually expected,<sup>46</sup> by the presence of vesicles, confirmed by SAXS

(Figure 2b) and the image in Figure 3b (GL, pH 6), both corresponding to a NP-free GL solution at pH 6. The TEM image of sample 3 (NPs GL pH6, Figure S 2a) confirms that nanoparticle size, morphology, structure and aggregation are not affected by the presence of the GL. However, GL can stabilize the nanoparticle surface, as commented above and as expected from the previous work performed on sophorolipids-stabilized iron oxide nanoparticles.<sup>55</sup> Light scattering experiments performed on sample S3 (Figure 3b), as well as its dim yellowish colour and aggregation state (Figure S 2a) are comparable to a control system composed of sophorolipid-stabilized iron oxide nanoparticles (sample S5, Figure 3a, Figure S 1, Figure 3b).

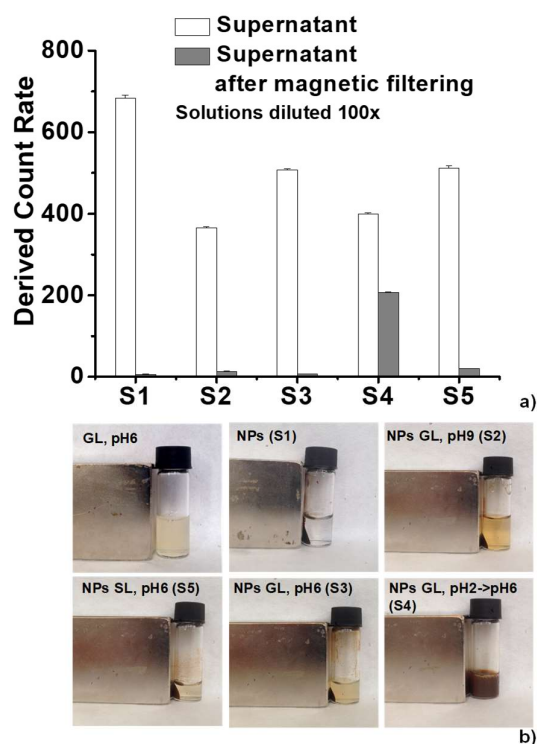


**Figure 3 – Light scattering data (a) and magnetically-assisted sedimentation images (b) for bare NPs (sample S1), GL-containing NPs at pH 9 (NPs GL, pH9, sample S2), GL-containing NPs at pH 6 (NPs GL, pH6, sample S3), GL-containing NPs at pH 6 after a transition at pH 2 (NPs GL, pH 2 → pH 6, sample S4), NPs-free GL solution at pH 6 (GL, pH6) and SLs-containing nanoparticle solution at pH 6 (NPs SL pH6, sample S5). Sample S5: control sample composed of sophorolipids-stabilized iron oxide NPs.<sup>55</sup>**

GLs are known to precipitate into a lamellar phase when the pH is lowered below 4,<sup>46</sup> also illustrated by the SAXS pattern recorded on a nanoparticle-free GL solution at pH 3.19 and shown in Figure 2b. In the last figure, two sharp diffraction peaks at  $q = 0.18 \text{ \AA}^{-1}$  and  $0.36 \text{ \AA}^{-1}$  overlaps the typical vesicle form factor profile; they respectively correspond to the first and second order interplanar distances lamellar stacking ( $d = 34.8 \text{ \AA}$  and  $d = 17.4 \text{ \AA}$ ). The cryo-TEM

analysis of a GL nanoparticle solution at pH below 4 displays the coexistence of nanoparticle clusters and flat lamellae (Figure S 3). Under these conditions, NPs can be easily removed by magnetically-assisted sedimentation, leaving a solid white precipitate in the vial. However, when pH is increased again to 6, the nanoparticle solution becomes extremely stable towards magnetically-assisted sedimentation: light scattering of sample S4 (Figure 3) indicates strong scattering before and after sedimentation. This is confirmed by the images showing the magnetically-sedimented undiluted sample (Figure 3b, sample S4): the dark solution indicates that most NPs are now stabilized. We anticipate that stability is observed over several hours of continuous exposure to the neodymium magnet.

Figure S 2b-d show that particle size ( $\sim 10$  nm) is unchanged compared to the GL-free NP solution and high magnification (Figure S 2b) and Fourier transform (Figure S 2c) indicate the crystallinity (Figure S 2d) of the particle with a typical distance of  $2.9 \text{ \AA}$ , attributed to the (220) plane of maghemite.

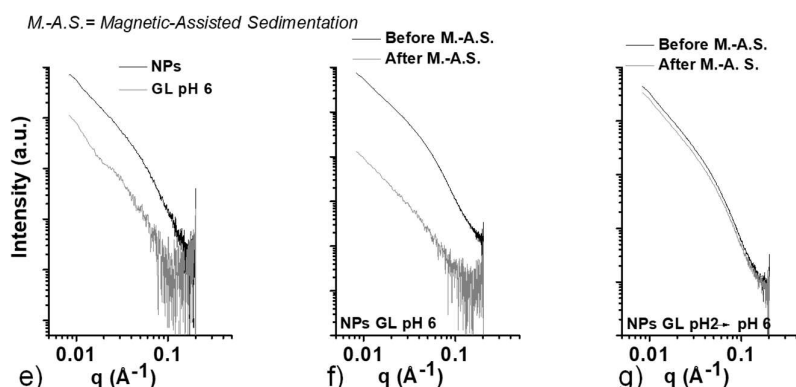
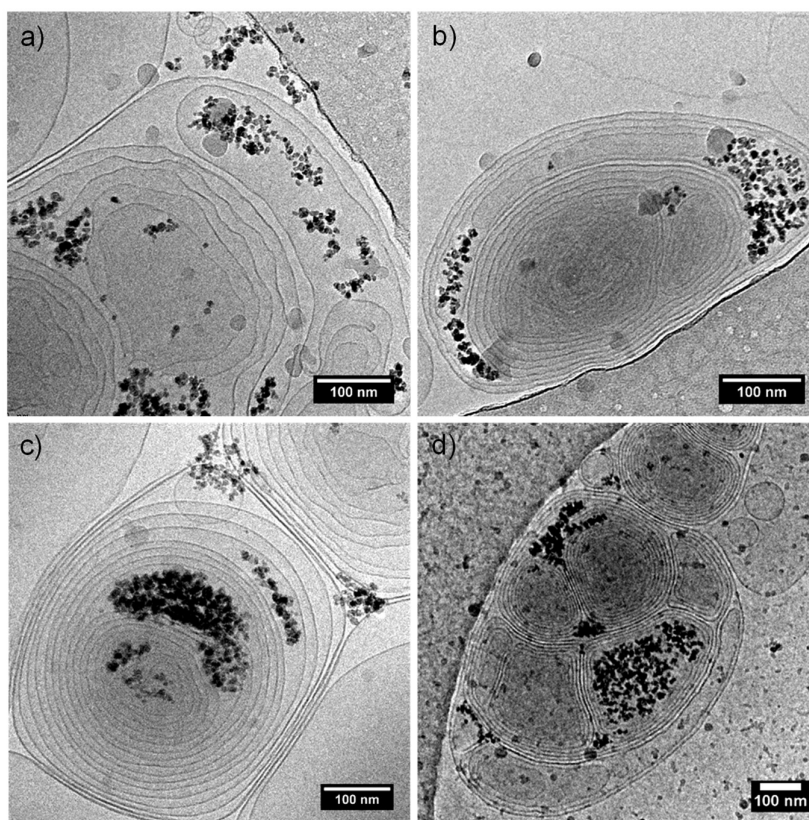
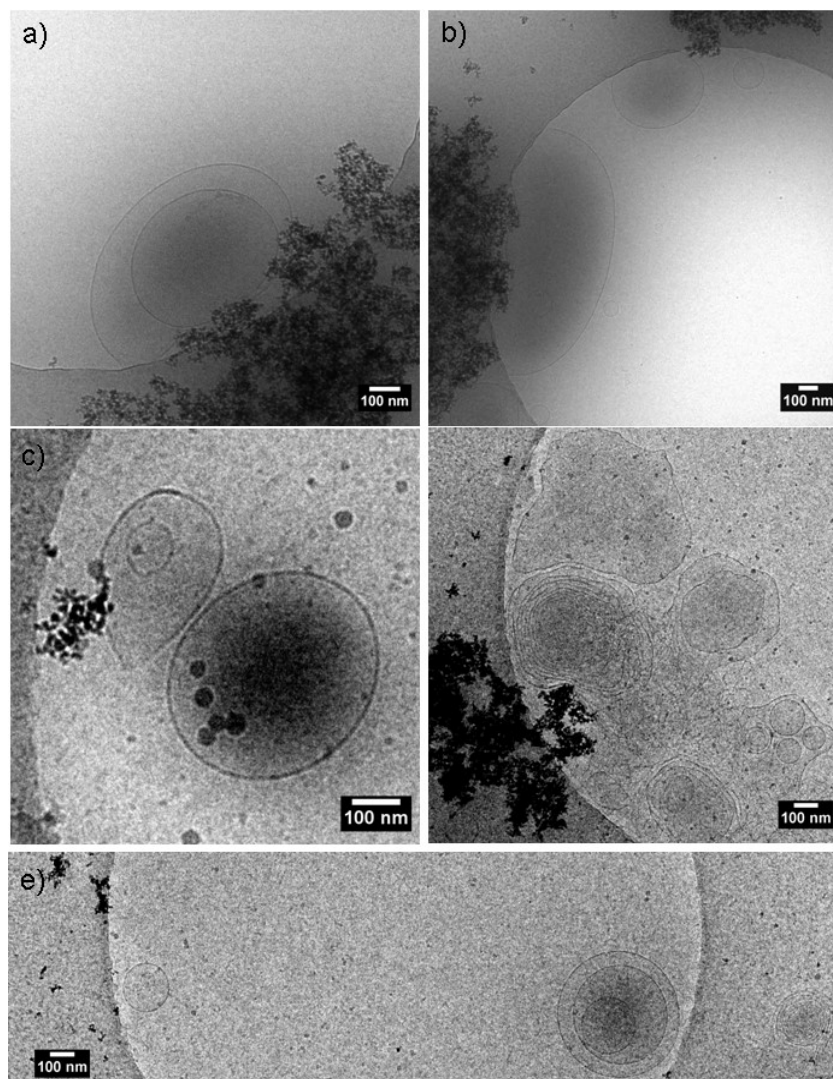


Figure 4 – a-d) Cryo-TEM images of NPs GL samples obtained after a pH jump (pH 9 →) pH 2 → pH 6 (NPs GL pH2→pH6, sample S4). e-g) Laboratory SAXS data recorded on e) bare NPs and NPs-free GLs at pH 6 (GL pH6), f) NPs GL samples at pH 6 directly adjusted from pH 9 (NPs GL pH6, sample S3) before (black curve) and after (grey curve) magnetically-assisted sedimentation, g) NPs GL samples at pH 6 adjusted from pH 9 after passing through pH 2 (NPs GL pH2→pH6, sample S4) before (black curve) and after (grey curve) magnetically-assisted sedimentation

Although GL adsorption is not excluded, the only surface passivating effect of GL cannot explain the colloidal stability at pH 6, because only a fraction of the NPs are in fact concerned, as already shown for sample S3 and control sample S5.<sup>55</sup> The remarkable stability

of the nanoparticle suspension is rather explained by the encapsulation of nanoparticle clusters within (mainly) multilamellar vesicles, as shown by cryo TEM experiments in Figure 4a-d. These data are statistically-confirmed by complementary SAXS experiments presented in Figure 4e-f: panel a) shows the typical signatures of bare NPs (black curve) and GL in solution at pH 6 (grey curve). The difference in the scattering intensity (although not in absolute scale) reveals the strong difference between NPs and GL in terms of contrast with the solvent (water). Additionally, the high-q region above  $0.1 \text{ \AA}^{-1}$  in the GL sample, although very noisy, shows the beginning of the form factor oscillation, which is very clear in the synchrotron-collected data on a larger q-scale (Figure 2b, pH 6.07). The highly stable pH 2  $\rightarrow$  pH 6 system (Sample S4, Figure 4g) shows that the signal is dominated by the NPs scattering before and after magnetically-assisted sedimentation, thus confirming that vesicles prevent their removal.

Finally, we have specifically verified the orthogonality between vesicle-formation and NPs dispersion: the pH 9  $\rightarrow$  pH 2  $\rightarrow$  pH 6 method is applied to a NPs-free GL solution and the corresponding cryo-TEM images in Figure S 4 confirm the presence of vesicles, and in particular of multilamellar vesicles. One can compare these results to the sample S3 (NPs GL pH 9  $\rightarrow$  pH 6), of which the cryo-TEM (Figure 5) and SAXS (Figure 4f) before (black curve) and after (grey curve) magnetically-assisted sedimentation indicate that the NPs are not preferentially encapsulated. Cryo-TEM shows that the NPs mostly aggregate around vesicles, while SAXS shows the typical signal of the NPs before and a pattern typical of the vesicles after magnetically-assisted sedimentation.



**Figure 5 – Cryo-TEM images of NPs GL samples prepared at pH 6 directly adjusted from pH 9 (NPs GL pH 6, sample S3)**

**Stability, control of the size distribution and quantification.** Time-dependent stability and size control of the encapsulated NPs are two important parameters for potential applications in nanomedicine and they are tested hereafter. Figure 6 shows the time stability of a GL solution mixed with NPs in the presence and absence of a magnet employing different approaches of encapsulation, but all performed using the pH jump (pH 9  $\rightarrow$  pH 2  $\rightarrow$  pH 6) process (sample 4). *Approach 1* and *approach 2* are, respectively, the vesicle-free NPs (sample S1) control and the manually-controlled pH jump (sample S4). Among the others, *approach 3* and *approach 4* respectively use extrusion and sonication after encapsulation, both being classical methods to control vesicle size in the 100 nm range (extrusion)<sup>52,53,54</sup> and below 50 nm (sonication).<sup>52</sup> Extrusion is also commonly employed to obtain unilamellar vesicles from multilamellar



vesicles. Finally, *approach 5* and *approach 6* are meant to perform the pH 2  $\rightarrow$  pH 6 jump either through a controlled NaOH injection (1 M NaOH at 0.5  $\mu$ L/min, *approach 5*) or through a very slow modification in pH (*approach 6*, using dialysis). Without vesicles (filled squares, Figure 6), the NPs sediment after several minutes in the absence of magnet, as expected from the Stokes law, while sedimentation is immediate upon use of a magnet. Whichever the approach of encapsulation, all vesicles-stabilized NPs solutions are similarly stable in time against sedimentation (Figure 6, left-hand): after 15 h, the transmittance is almost constant, while the vesicle-free control is clear. In the presence of a magnet (Figure 6, right-hand), none of the solution shows the same immediate collapse as found in the vesicle-free control (black squares), thus indicating that encapsulation is always successful. However, after 2 h of exposure to the magnet, the transmission is not equivalent among the tested solutions, probably indicating a disparity in terms of the encapsulation efficiency. Extruded, sonicated and controlled pH jump (respectively, approach 3, 4 and 5) seem to be the most efficient approaches.

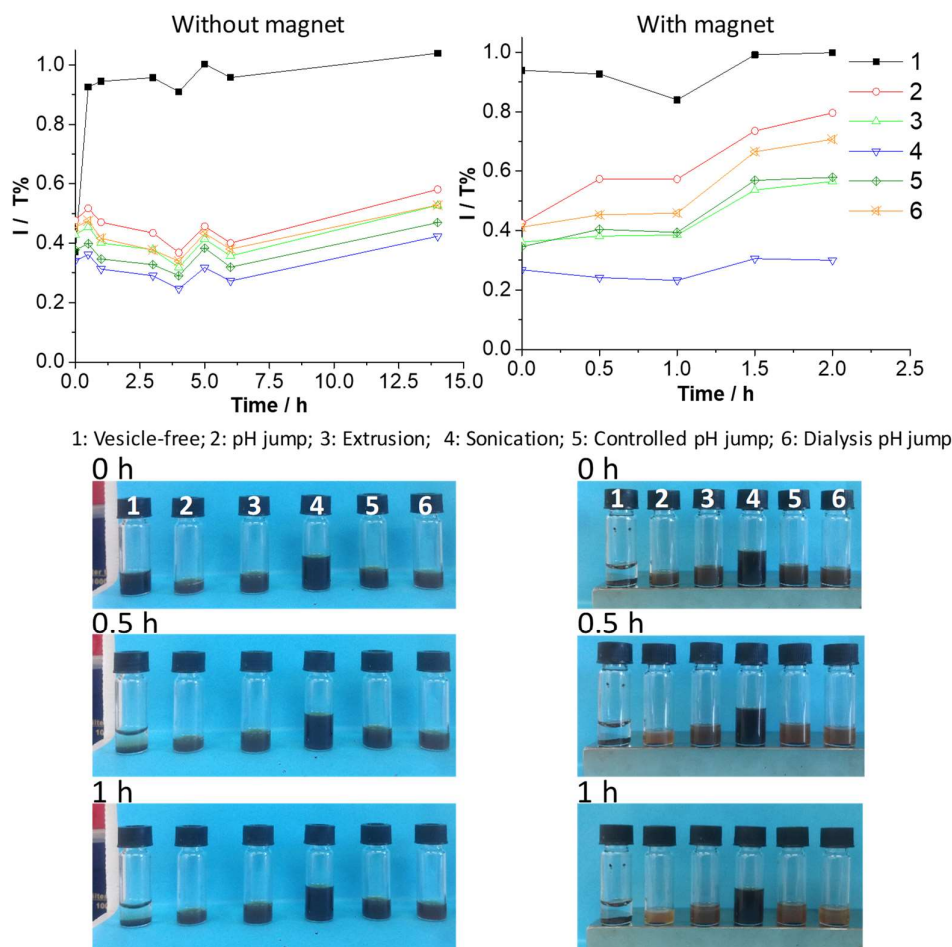


**Figure 6 – Time-dependent stability of NPs GL pH 2  $\rightarrow$  pH 6 (sample S4) using approaches 1 through 6**

(refer to figure and materials and methods section). Data on the left-hand side refer to simple decantation (no magnet) while data on the right-hand side are acquire using magnetically-assisted sedimentation of the solution (vials sit on a neodymium, as shown on figure)

Extrusion is known to be a severe process that can destabilize the most stable nanoparticle systems.<sup>56</sup> Vesicles-stabilized NPs prepared by pH jump provide an ultra-stable dispersion of NPs upon extrusion (*approach 3*). Video 1 shows that a vesicles-stabilized NP solution can be extruded repeatedly (we tested up to ten cycles) without aggregation of the NP onto the filter, while a vesicle-free NP solution cannot be extruded once (Video 2). The advantage of employing various sample preparation approaches is the possibility to control the vesicles size distribution, as formulated theoretically in the development of nonequilibrium compartments.<sup>28</sup> Figure 7 shows the autocorrelation function and the corresponding number distribution of the (vesicle-free) iron oxide NPs solution (in red), the (NPs-free) GL vesicle solution obtained through the pH jump (in green) and the vesicles-stabilized NPs solution (in black) obtained with approaches 2 through 6. Both manual and dialysis pH jump approaches provide a heterogenous dispersion of vesicles and NPs with a broad size distribution, in agreement with the cryo-TEM images of sample 4 in Figure 4. On the contrary, extrusion, sonication and controlled pH jump provide a homogeneous set of NPs dispersion, of which the size distribution can be tuned between 50 nm (sonication) and 500 nm (controlled pH jump). In particular, the comparison between the autocorrelation function of the NPs-free vesicles and the vesicles-stabilized NPs systems in the controlled pH jump approach clearly shows that the size distribution of the latter is controlled by the process of vesicle formation. Selected cryo-TEM images for the sonication and extrusion processes are also shown in Figure 7 (right-hand side) to support the DLS data. Cryo-TEM shows that sonication produces vesicles between 20 nm and 50 nm, while extrusion produces vesicles of size contained between about 100 nm and 300 nm. In both cases the average size and size distribution are in good agreement with the DLs data. White arrow in the cryo-TEM image recorded on the extruded vesicles-stabilized NPs system also shows a typical vesicle highly loaded with iron oxide NPs.

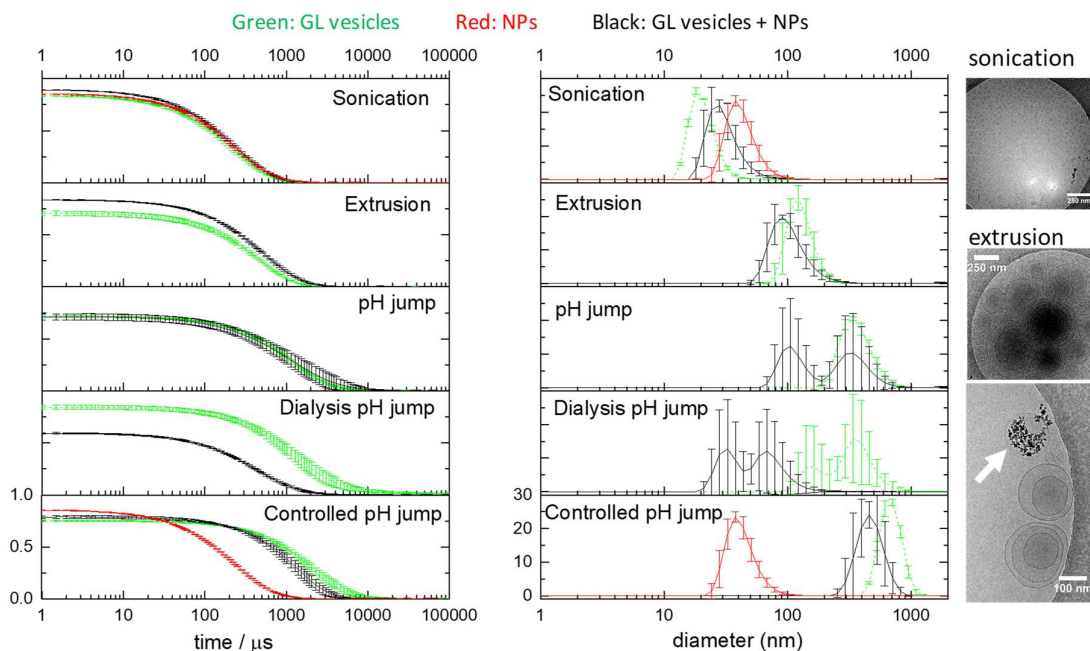


**Figure 7 – Autocorrelation functions (left-hand panels) and number size distribution (right-hand panels) of NPs GL pH 2 → pH 6 solutions (sample 4) prepared using approaches 2 through 5, respectively referring to (manual) pH jump, extrusion, sonication, controlled pH jump and dialysis pH jump. The experimental detail of each approach is provided in the materials and methods section. To support the DLS data on size control, cryo-TEM images are provided on the right-hand side for the sonication and extrusion methods. White arrow point at a typical vesicle highly loaded with iron oxide NPs.**

Vesicles-stabilized NPs can be reproducibly prepared by the pH jump approach, which controls a lamellar-to-vesicle phase transition when passing from highly acidic pH (it works between 2 and 4) to pH ~6. Stability and size control of the NP-encapsulated vesicles depends on the method the lamellar-to-vesicle phase transition line is crossed. This behaviour identifies a kinetically controlled process, where the non-equilibrium NPs dispersion is randomly encapsulated during the process of bilayer folding into vesicles. To estimate the repeatability of the encapsulation process and the loading efficiency, the manual pH jump experiment (sample S4 in Figure 3, approach 2 in Figure 6) was repeated twenty times. By a simple gravimetric method, we find an encapsulation efficiency of  $59.2 \pm 16.0$  %. These values are obtained by weighting the mass of the NPs collected through the magnetically-assisted sedimentation with respect to the total mass of the initial NPs load. Figure S 5 qualitatively shows two systems, where the NPs retain rate in solution is in the order of 50 % (Figure S 5b) and above 50 % (Figure S 5c), and where Figure S 5a shows the control image of a typical NPs-free GL vesicle solution. Considering the broad variation across experiments in the

encapsulation efficiency ( $\pm 16.0\%$ ), we did not estimate useful to perform more precise measurements. However, loading efficiency values above 50 % can be compared with the highest values reported in the literature for magnetoliposome systems, with encapsulation occurring both in the lumen and bilayer.<sup>57,58,59,60</sup>

**Understanding the uneven encapsulation profile.** At the moment, the only hypothesis supporting the encapsulation of magnetic iron oxide NPs (magnetoliposomes) is the lamellar-to-vesicle transition occurring during the pH 2  $\rightarrow$  pH 6 jump process, a similar process described for vesosomes from cochleate cylinders,<sup>32</sup> or in more standard thin film hydration.<sup>13</sup> In this work, such a mechanism is strongly suggested by the fact that both unilamellar and multilamellar vesicles are produced during the micelles-to-vesicle (pH 9  $\rightarrow$  pH 6)<sup>46</sup> and lamellar-to-vesicle (pH 9  $\rightarrow$  pH 2  $\rightarrow$  pH 6, Figure S 4) transition. The folding process of the bilayer membrane into closed objects during the pH 2  $\rightarrow$  pH 6 jump, and which was already shown to be driven by temperature for GL,<sup>46</sup> internalizes the NPs in solution. Nanoparticles are locally aggregated but their volumetric distribution is homogeneous at a macroscopic scale due to previous sonication (in the absence of GL vesicles) and stirring (in the presence of GL vesicles). Nonetheless, the variability in loading efficiency is quite high ( $\pm 16\%$ ), a fact which can be explained by several factors. Figure 6 and Figure 7 show the impact of the encapsulation process on the stability and size distribution, where the finest control provides the most stable systems. Manual variation, although quite robust and easy to perform, obviously suffers from an intrinsic variability, especially in a kinetically controlled process. Locally, cryo-TEM shows a coexistence of heavily-loaded vesicles and empty vesicles, rather than a homogeneous encapsulation event. Interestingly, a similar behaviour was reported by Bothun<sup>59</sup> and by Luisi,<sup>13</sup> respectively on water-dispersible magnetite and iron-loaded ferritin, the latter using a statistical approach employing cryo-TEM. Unfortunately, any attempt to improve the homogeneity of the encapsulation among the vesicles, for instance using different molarities (e.g., 1 M and 0.1 M) of NaOH, was vain, suggesting other mechanisms behind the encapsulation phenomenon.

To better understand whether or not the uneven encapsulation profile is specific to this system, we have decided to repeat the pH-driven encapsulation experiment using ferritin nanocages containing an iron core. Luisi et al.<sup>13</sup> have demonstrated that encapsulation of ferritin (performed through thin film hydration and ethanol injection) in the lumen of 1-palmitoyl-2-oleoyl-sn-glycero-3-phosphatidylcholine vesicles is not described by a classical Poisson-Boltzmann distribution function, but rather by a small fraction of heavily-loaded vesicles surrounded by empty ones. (Fe4800)AfFtn, characterized in ref. 51, is a water-dispersible

material similar to the one employed by Luisi et al.;<sup>13</sup> it is characterized by an iron core (4800 iron atoms) of 8 nm enclosed in a proteic cage of 13 nm in diameter.

(Fe4800)AfFtn is encapsulated in GL vesicles using three main approaches: *manual pH jump (approach 2)*, *controlled pH jump (approach 5)* and *extrusion (approach 3)*. These experiments are all analyzed by cryo-TEM presented in Figure 8. Typical (Fe4800)AfFtn is indicated by the white arrows in Figure 8a1,b2. Irrespective of the encapsulation approach, we systematically observe empty, or close to empty, vesicles coexisting with loaded vesicles (Figure 8a1,b1,c1), and in few cases, highly loaded vesicles (a thorough statistical analysis is however out of the scope of this work). In particular, Figure 8b3,b4,c2,c3 show the side-to-side coexistence of extremely crowded vesicles next to empty ones, as concluded by Luisi et al.<sup>13</sup> Whether there may be an influence of the encapsulation approach or not, we do not have enough statistically-meaningful data in our possession to conclude on this point, but this is not excluded, as shown by cryo-TEM images corresponding to the extrusion approach. Figure 8c1, for instance, shows a typical example of a large burst vesicle (arrow 1), from which (Fe4800)AfFtn particles are free of diffusing from inside to outside and vice versa. One can also observe small portions of a smaller vesicle being heavily loaded (arrow 2). We did not observe similar events occurring in the manual and controlled pH jump. This can be explained by the reduction in vesicle size polydispersity (Figure 7) after extrusion, a fact that can involve vesicle bursting and intervesicular fusion.

These experiments show that the phase change encapsulation approach developed in this work using the pH-responsive GL provides the same uneven distribution profile of the ferritin nanocages within the lumen of the vesicular compartments, similarly to what was described in ref. 13. To this regard, the data shown in Figure 4 are neither specific to the encapsulation of iron oxide NPs nor to the pH-driven encapsulation method, but they seem to follow an accepted, although not fully understood, distribution profile, which cannot be described by a standard Poisson-Boltzmann distribution function. On another level, the encapsulation of (Fe4800)AfFtn also suggest that the method developed in this work could be extended to the encapsulation of a broader range of water-stable nanocolloids.

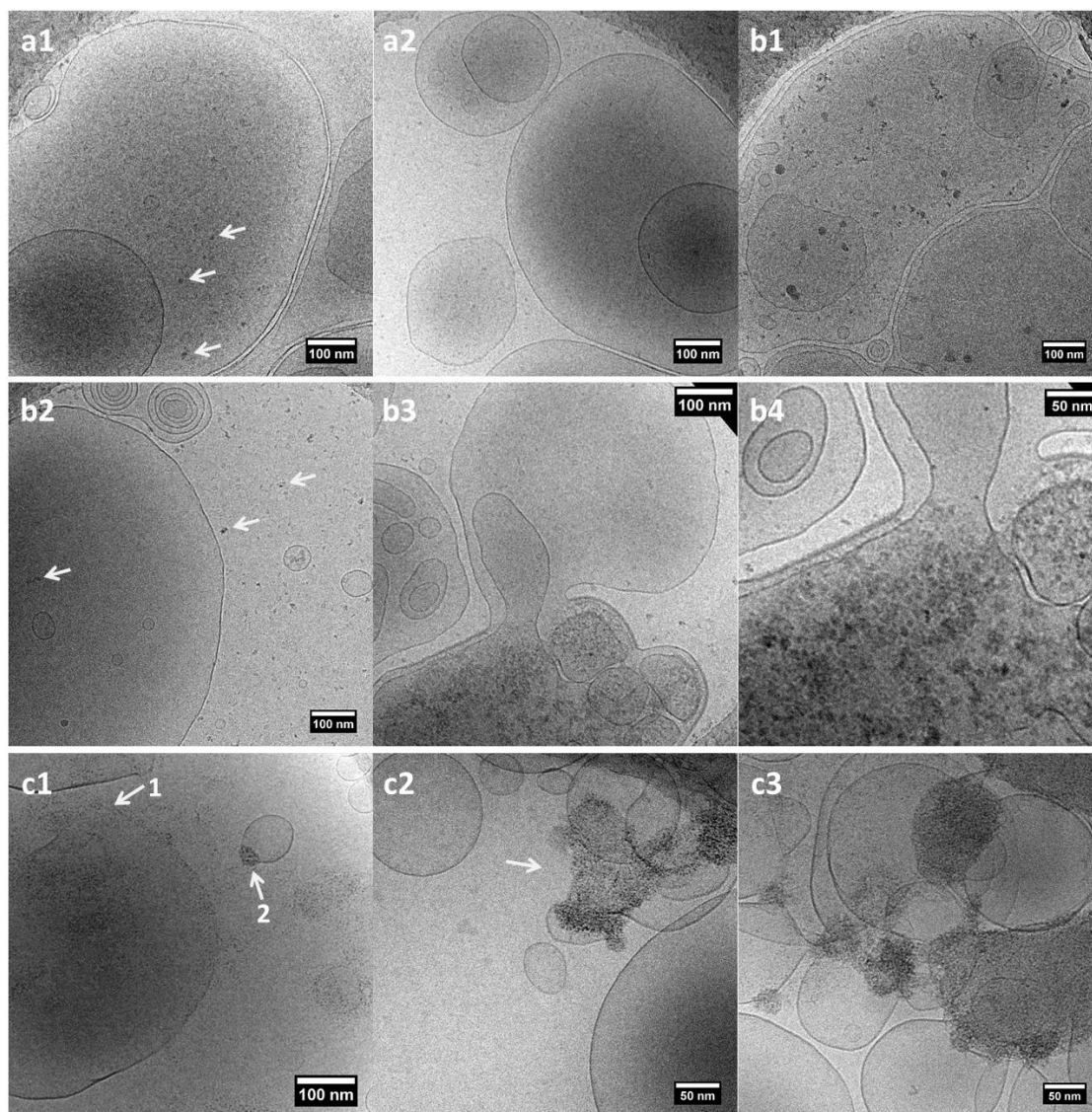


Figure 8 - Cryo-TEM images of GL samples containing Ferritin-4800 (average diameter of 13 nm) obtained after a pH jump (pH 7.4 → pH 3.9 → pH 6. The following approaches (please refer to the method section for more information) are employed: a1-a2) controlled pH jump; b1-b4) manual pH jump; c1-c3) extrusion after manual pH jump.

### Extending the pH-jump encapsulation to aqueous dispersions of hydrophobic oleic-stabilized upconverting nanoparticles

UCNP are interesting colloids with a wide variety of applications for their ability to absorb energy in the near infrared (NIR) and convert it to visible light. The most important concerns the field of bioimaging because living tissues are transparent in the NIR.<sup>31</sup> The actual synthesis procedure occurs in organic media, from which the UCNPs result in poor water

solubility due to their hydrophobic coating. Strategies to make UCNP hydrosoluble, which generally consists in tedious ligand exchange procedures, are crucial for their application in the biomedical field. In this sense, it could be very interesting to avoid the ligand exchange step and to directly encapsulate the UCNP bearing their original hydrophobic coating. The sonication-assisted phase change method developed in the previous section for bare iron oxide NPs could be an interesting alternative to more classical encapsulation approaches,<sup>25</sup> which would require surface engineering steps to make UCNP water-dispersible. Furthermore, as shown in many magnetoliposome systems, stable NPs bearing a hydrophobic coating classically partition in the lipid bilayer of the vesicles,<sup>1,9,15,16,56,57</sup> and in general only the employment of surfactants, which guarantee oil-water phase transfer, forces them to aggregates in the lumen.<sup>21</sup> Otherwise, standard hydrophilic stabilizers (e.g., citric acid, polymers) are used to surface stabilizers that help them aggregate in the lumen.<sup>16,57,59,60</sup> In this section, we make the hypothesis that the sonication-assisted phase-change method employing the pH-responsive GL can also be used to encapsulate hydrophobic colloids under the same conditions employed to form magnetoliposomes. We employ UCNP used with an average diameter between 20 nm and 40 nm; they are composed of NaYF<sub>4</sub>:Yb/Er and NaYF<sub>4</sub>:Yb/Tm, both coated with oleic acid. Due to their oleic coating, they aggregate in water, either sedimenting or immediately adsorbing on the glass vial.

NaYF<sub>4</sub>:Yb/Er and NaYF<sub>4</sub>:Yb/Tm UCNP are prepared according to a standard procedure;<sup>50</sup> their typical XRD pattern (Figure S 6a) depicts a classical mixture of hexagonal and cubic crystal structures, while the corresponding TEM micrographs (Figure S 6b) show a polydisperse set of sub-50 nm nanoparticles (size distribution is given in Figure S 6c). The oleic hydrophobic coating is shown by DTA analysis (red profile in Figure S 6e). Given their hydrophobic coating, they are hardly water-dispersible, unless sonication is applied. In this case, the UCNP powder mix with water but it precipitates within the order of minutes, as shown by both light scattering (Figure 9a) and photoluminescence spectroscopy (Figure 9b,c). When the UCNP are added to a GL solution and are submitted to a *manual pH jump (approach 2)*, we find a prompt dispersibility in water and an enhanced colloidal stability. Combination of light scattering (Figure 9a, sensitive to both nanoparticles and vesicles), with photoluminescence spectroscopy (Figure 9b,d, only sensitive to UCNP), show stability of the encapsulated UCNP in solution up to one hour. The stability is also confirmed by photoluminescence spectroscopy data recorded on a series of centrifuged samples: encapsulated UCNP emit significant amount of light up to 2000 rpm for as long as 1 min of centrifugation time (Figure 9e). These results are independent of the nature of doping element (Er or Tm). These data are also completed by

XRD and DTA results (Figure S 6d,e) showing that encapsulation does not affect the crystalline structure of the UCNP and, most importantly, that the passivating hydrophobic layer is not exchanged with GL. The typical DTA signature of GL (black curve in Figure S 6e) is different than the signature of the hydrophobic coating in both as-synthesized and encapsulated UNCP samples (Figure S 6e).

These experiments show that hydrophobic, aggregated, UCNPs can easily be dispersed in an aqueous environment assisted by sonication followed by exposure to GL and employing the phase change method. Absence of oleic-GL ligand exchange shown by DTA indicates that the stabilization process mainly occurs by their encapsulation in the GL vesicles, as shown by cryo-TEM (arrows 1 and 2 point at encapsulated NaYF<sub>4</sub>:Yb/Er particles in Figure 9f,g). The colloidal stability, tested here up to one hour, is impressive if compared to the control system composed of oleic acid coated UCNP in water, although less long-lasting than what we have found for iron oxide NPs. At the moment, we do not have a clear explanation for this, but the hydrophobic coating should certainly favour phase separation more than the bare surface of iron oxide NPs, and cryo-TEM data (arrow 3 in Figure 9g) also shows that it is not uncommon to find aggregated UCNP clusters outside of the vesicles.



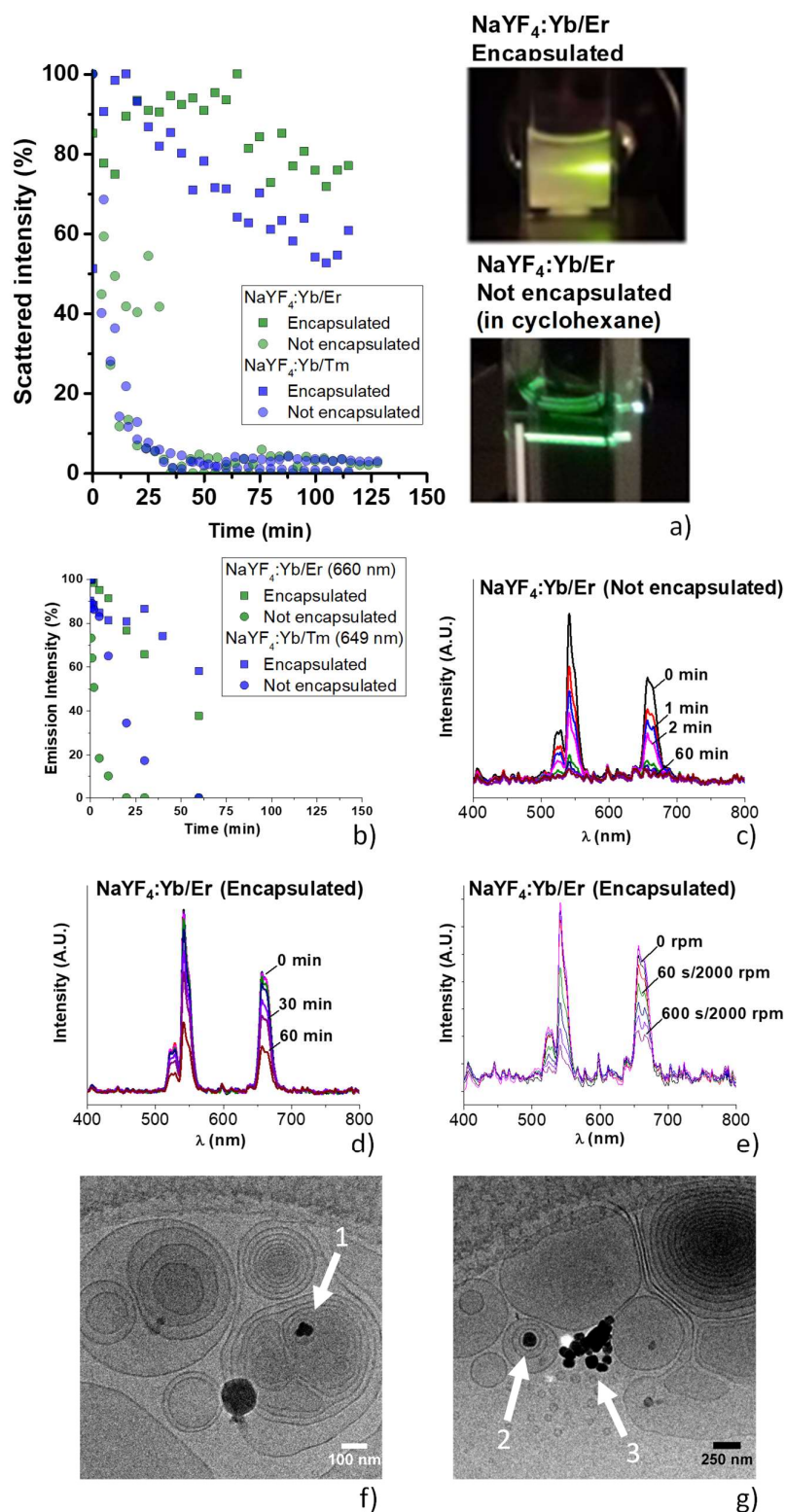


Figure 9 – Sedimentation of static (0 rpm) GL-free and GL-encapsulated NaYF<sub>4</sub>:Yb/Ln (Ln= Er or Tm) UCNP samples measured by a) light scattering ( $\lambda = 633$  nm,  $\theta = 90^\circ$ , constant shutter opening, two replica are presented) and b) photoluminescence spectroscopy ( $\lambda_{exc} = 980$  nm), of which the time evolution of the

emission spectra for free sedimentation of NaYF<sub>4</sub>:Yb/Er are given in c) (nanoparticles in water) and d) (encapsulated nanoparticles). Pictures in a) correspond to irradiated ( $\lambda_{exc}= 980$  nm) NaYF<sub>4</sub>:Yb/Er UCNPs dispersed in GL vesicles (top picture) and cyclohexane (bottom image). e) Time evolution of the photoluminescence emission ( $\lambda_{exc}= 980$  nm) of encapsulated NaYF<sub>4</sub>:Yb/Er UCNPs with forced sedimentation (centrifugation at 2000 rpm). f-g) Typical cryo-TEM image of an encapsulated (arrows 1, 2) and non-encapsulated (arrow 3) NaYF<sub>4</sub>:Yb/Er sample

The results presented in this work are summarized in Figure 10. Non-equilibrium entrapment of metastable functional nanoparticles can occur via the same lamellar-to-vesicle phase change process assisted by sonication. In this work, we successfully tested the encapsulation of bare (uncoated) iron oxide NPs and oleic acid coated UCNPs. Iron-loaded ferritin nanocages were also encapsulated with the goal of understanding the origin of the uneven distribution of the colloids within the vesicular compartments, in comparison to the Luisi's encapsulation experiments.<sup>13</sup> However, these preliminary data suggest that stable colloids could also be encapsulated through the same method. As a general remark, it seems that this approach could be potentially extended to a broad class of nanocolloids both stable and unstable in water, including those bearing a hydrophobic coating. This is an interesting point compared to the literature, where efficient encapsulation in the vesicle lumen commonly requires surface stabilization of the nanoparticles via hydrophilic coatings, while hydrophobic coatings tend to partition the nanoparticles in the lipid bilayer.<sup>16,57</sup> In terms of encapsulation efficiency, the highest standards in the literature settle around 50%, but with the clear distinction between hydrophilic and hydrophobic colloids, respectively encapsulated in the lumen and bilayer.<sup>16,57</sup> An interesting work by Amstad et al.<sup>56</sup> shows that iron oxide nanoparticles bearing a stable catechol-based hydrophobic coating partition in the bilayer membrane with an encapsulation efficiency of about 30%, while labile carboxylic hydrophobic induce uncontrolled NPs aggregation outside the vesicles and stable catechol-based hydrophilic coatings induce encapsulation in the lumen. Uncoated NPs aggregates can actually be encapsulated in the lumen, but the efficiency is very low (< 10%) compared to the use of stable colloids bearing a hydrophilic coating and for which efficiency can reach 50%.<sup>60</sup>

Our data collected with the phase-change method using GL show that the encapsulation efficiencies in the lumen can reach values as high as 70% on uncoated iron oxide NPs aggregates (estimated through gravimetric methods), or about 50% (after 1 h) using hydrophobic oleic acid coated UCNPs (estimated with emission luminescence spectroscopy). The values settle among the highest found in the literature and they also show that the

sonication-assisted phase change method of encapsulation in the lumen can be easily applied to a broad range of as-prepared colloids, for which the classical steps involving the tedious ligand exchange process could be possibly avoided. Nonetheless, despite the fact that our data do not suggest that surface chemistry has a major impact on the vesicle-formation process from the lamellar phase above pH 4, we cannot exclude an impact on the other features, like the encapsulation efficiency, the NPs distribution within the vesicles or effects on the vesicle size and stability, as found by others.<sup>56</sup> Furthermore, the average encapsulation efficiency found here settles around 60% with very broad variability ( $\pm 16\%$ ). It is also not excluded that the latter could be influenced by the surface chemistry of the nanocolloids but also by the process of bringing the NPs out of equilibrium through sonication, a parameter of which the role should be better explored in future work. Finally, for realistic applications, the stability of the GL vesicles in a broader pH range, especially above pH 6-7, and in cell culture media must be studied in more details.

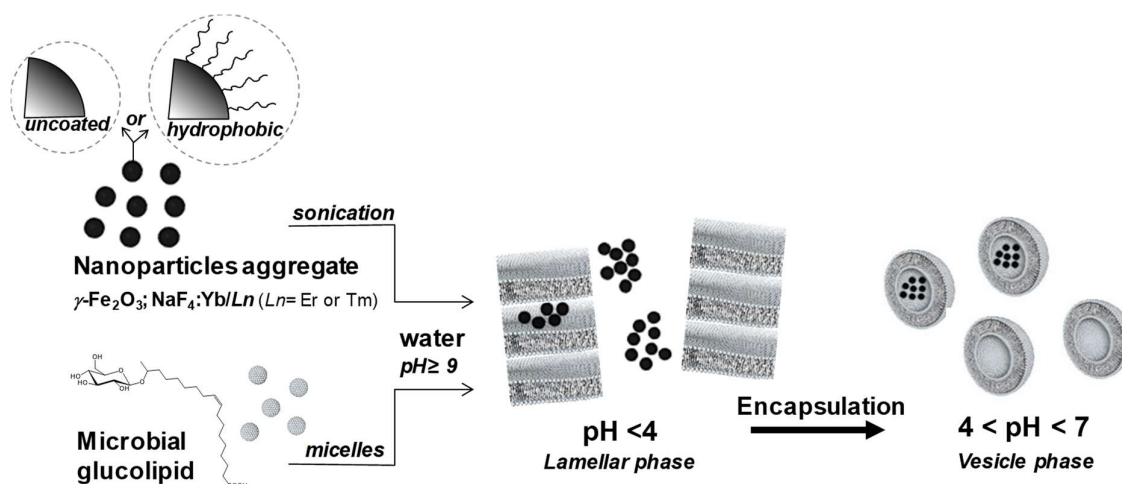


**Figure 10 – NPs encapsulation into vesicles: the pH jump method used in this work start from a glucolipid solution above pH 9 (micellar) and then lowered to pH < 4 (lamellar). Sonication assists dispersion of NPs, which coexist with the micellar and lamellar phase, according to the pH value. The cartoon at pH < 4 shows that clusters of NPs coexist with the lamellar phase, although exact positioning of the clusters (intra or interlamellar) is still unclear. The lamellar-to-vesicle transition occurs above pH 4 and it is responsible for the encapsulation process, resulting a small fraction of heavily-loaded vesicles.**

## Conclusion

This paper shows the possibility to form magnetoliposomes from a biobased lipid source simply using pH as a physico-chemical trigger in water at room temperature. The vesicle-forming properties of a new family of microbial glycolipids is exploited to encapsulate

magnetite ( $\gamma$ -Fe<sub>2</sub>O<sub>3</sub>) NPs within glucolipid (GLs) vesicles. More precisely, acidic C18:1 GLs, produced by *S. bombicola* strain *AugtB1* are compounds constituted by a  $\beta$ -D-glucose headgroup linked through a glycosidic bond to the subterminal carbon (C17) of hydroxylated oleic acid, thus leaving a free-standing COOH group. As shown by SAXS and cryo-TEM, this compound mainly forms micelles at neutral to basic pH, vesicles between pH 4 and pH 6 and a lamellar phase below pH 4. Direct exploitation of the lamellar-mediated vesicle-forming mechanism when the pH is increased back from below 4 to pH 6 leads to an encapsulation of NPs simultaneously dispersed in the GL solution. Cryo-TEM shows the presence of few but densely-crowded magnetoliposomes. We have repeated the encapsulation experiment using iron-loaded ferritin (Fe4800)AfFn and we do obtain analogous results: very few heavily loaded vesicles coexisting with empty ones. A similar distribution profile was reported for ferritin nanocages encapsulated within the lumen of liposomes obtained from standard phospholipids using more classical embedding approaches (ethanol injection, thin film hydration). The analogy between our data and the literature for the specific ferritin system suggests that the uneven distribution of NPs within vesicles found in this work does not depend on our conditions of work, but it seems to be a more general, yet misunderstood, phenomenon.

In our experiments, we evaluate an encapsulation efficiency in the lumen of about 60%, a value which settles among the highest in the literature, especially if compared to the use of either uncoated or hydrophobic nanoparticles, whereas the former have shown to be encapsulated in the lumen but with efficiencies below 10% and the latter are generally encapsulated in the lipid bilayer. Nonetheless, variability is quite high ( $\pm 16\%$ ), a fact which can depend both on the surface chemistry of the NPs and, above all, on the sonication step required to bring the NPs out of equilibrium. Although at the moment it is not clear how to achieve a precise control of the encapsulation efficiency, we were able to control the average diameter between tens and several hundred of nanometers by varying the encapsulation process, still keeping the same pH change approach. Sonication was found to provide the smallest vesicle size while controlled pH change provides the largest vesicles. The extrusion experiments, besides stabilizing the average vesicle diameter around 100 nm, nicely demonstrate the high stability of the magnetoliposomes towards multiple extrusion cycles.

Besides unprotected iron oxide nanoparticles, using the simple phase change encapsulation process in the presence of GL, we were able to encapsulate and stabilize two upconverting sub-50 nm nanoparticles systems composed of oleic-acid coated NaYF<sub>4</sub>:Yb/Ln (Ln= Er or Tm). These water-insoluble materials could be dispersed in water and stabilized up to 50% (according to luminescence emission spectroscopy) in the order of one hour under static

sedimentation conditions, and in the order of minutes under centrifugation at 2000 rpm. These results suggest that the present method of encapsulation in the lumen may be applied to a broad range of colloids, for which typical, but tedious, ligand exchange steps could be potentially avoided.

## **Acknowledgements**

The research leading to these results has received funding from the European Community's Seventh Framework Programme (FP7/2007-2013) under Grant Agreement n° Biosurfing/289219 and a national IWT innovation mandate grant with project number 140917. This work was also supported by Spanish Government (MINECO, project MAT2015-64139-C4-2-R) and Universitat Jaume I (UJI-B2018-71 project). The mobility of LVR was financially supported by The Research Foundation - Flanders (FWO) through an international mobility scholarship. The mobility of F. Guzzetta was supported by COST Actions of the European Commission (COST-STSM-ECOST-STSM-MP1202-010916-079377) and Balaguer Gonet Foundation. Generalitat Valenciana is acknowledged for the PhD fellowship of FG. NTU-Northwestern Institute for Nanomedicine (Singapore) is kindly acknowledged for funding SL at School of Chemical and Biomedical Engineering. Serveis Centrals d'Instrumentació Científica from UJI is also acknowledged for instrumental facilities. The SAXS experiments were performed on beamline ID02 at the European Synchrotron Radiation Facility (ESRF), Grenoble, France. We are grateful to Dr. Sylvain Prévost, our local contact at the ESRF for providing assistance in using beamline ID02.

## **Keywords**

Biosurfactants; Encapsulation; Glycolipids; Magnetoliposomes; Vesicle

- <sup>1</sup> M. R Preiss, G. D. Bothun, Stimuli-responsive liposome nanoparticle Assemblies, *Expert Opin. Drug Deliv.*, **2011**, 8, 1025-1040
- <sup>2</sup> K. Hong, D. S. Friend, C. G. Glabe, D. Papahadjopoulos Liposomes Containing Colloidal Gold Are A Useful Probe Of Liposome-Cell Interactions, *Biochim. Biophys. Acta*, **1983**, 732, 320-323
- <sup>3</sup> H. Kiwada, J. Sato, S. Yamada, Y. Kato, Feasibility of Magnetic Liposomes as a Targeting Device for Drugs, *Chem. Pharm. Bull.*, **1986**, 34, 4253-4258
- <sup>4</sup> M. De Cuyper, M. Joniau Magnetoliposomes Formation and structural characterization, *Eur. Biophys. J.*, **1988**, 15, 311-319
- <sup>5</sup> C.-S. Chen, J. Yao, R. A. Durst, Liposome encapsulation of fluorescent nanoparticles: Quantum dots and silica nanoparticles, *J. Nanopar. Res.*, **2006**, 8, 1033–1038
- <sup>6</sup> C. Sangregorio, J. K. Wiemann, C. J. O'Connor, Z. Rosenzweig, A new method for the synthesis of magnetoliposomes, *J. Appl. Phys.*, **1999**, 85, 5699
- <sup>7</sup> A. Wijaya, K. Hamad-Schifferli, High-Density Encapsulation of Fe<sub>3</sub>O<sub>4</sub> Nanoparticles in Lipid Vesicles, *Langmuir*, **2007**, 23, 9546-9550
- <sup>8</sup> R. R. Sawant, V. P. Torchilin, Liposomes as ‘smart’ pharmaceutical nanocarriers, *Soft Matter*, **2010**, 6, 4026–4044
- <sup>9</sup> E. Reimhult, Nanoparticle-triggered release from lipid membrane vesicles, *New Biotechnol.*, **2015**, 32, 665-672
- <sup>10</sup> R. T. Pearson, M. Avila-Olias, A. S. Joseph, S. Nyberg, G. Battaglia, Smart Polymersomes: Formation, Characterisation and Applications, in *Smart Materials for Drug Delivery: Vol. 1*, 2013, 179-207, RSC Smart Materials No. 2, Ed. C. Alvarez-Lorenzo and A. Concheiro, The Royal Society of Chemistry
- <sup>11</sup> R. Chandrawati, F. Caruso, Biomimetic Liposome- and Polymersome-Based Multicompartmentalized Assemblies, *Langmuir*, **2012**, 28, 13798–13807
- <sup>12</sup> G. Fuks, R. Mayap Talom, F. Gauffre, Biohybrid block copolymers: towards functional micelles and vesicles, *Chem. Soc. Rev.*, **2011**, 40, 2475–2493
- <sup>13</sup> P. L. Luisi, M. Allegretti, T. P. De Souza, F. Steiniger, A. Fahr, P. Stano, Spontaneous protein crowding in liposomes: a new vista for the origin of cellular metabolism, *ChemBioChem*, **2010**, 11, 1989–1992
- <sup>14</sup> S. Mann, J. P. Hannington, Formation of iron-oxides in unilamellar vesicles. *J. Colloid Interface Sci.*, **1988**, 122, 326–335
- <sup>15</sup> C. Bonnaud, C. A. Monnier, D. Demurtas, C. Jud, D. Vanhecke, X. Montet, R. Hovius, M. Lattuada, B. Rothen-Rutishauser, A. Petri-Fink, Insertion of nanoparticle clusters into vesicle bilayers. *ACS Nano* 2014, 8, 3451-3460
- <sup>16</sup> C. A. Monnier, D. Burnand, B. Rothen-Rutishauser, M. Lattuada, A. Petri-Fink, Magnetoliposomes: opportunities and challenges, *Eur. J. Nanomed.*, **2014**, 6, 201–215
- <sup>17</sup> 1,2-dimyristoyl-sn-glycero-3-phosphoglycerol
- <sup>18</sup> 1,2-dipalmitoyl-sn-glycero-3-phosphoglycerol
- <sup>19</sup> E. Viroonchatapan, M. Ueno, H. Sato, I. Adachi, H. Nagai, K. Tazawa, I. Horikoshi, Preparation and Characterization of Dextran Magnetite-Incorporated Thermosensitive Liposomes: An on-line Flow System for Quantifying Magnetic Responsiveness, *J. Pharm. Res.*, **1995**, 12, 1176-1183
- <sup>20</sup> F. Szoka, Jr., D. Papahadjopoulos, Procedure for preparation of liposomes with large internal aqueous space and high capture by reverse-phase evaporation, *Proc. Natl. Acad. Sci. U.S.A.*, **1978**, 75, 4194-4198

- <sup>21</sup> G. Beaune, M. Levy, S. Neveu, F. Gazeau, C. Wilhelm, C. Ménager, Different localizations of hydrophobic magnetic nanoparticles within vesicles trigger their efficiency as magnetic nano-heaters, *Soft Matter*, **2011**, 7, 6248
- <sup>22</sup> S. Zheng, Y. Zheng, R. L. Beissinger, R. Fresco, Microencapsulation of hemoglobin in liposomes using a double emulsion, film dehydration rehydration approach, *Biochim. Biophys. Acta Biomembr.*, **1994**, 1196, 123-130
- <sup>23</sup> Ana Rita O. Rodrigues, Pedro M.F. Mendes, Pedro M.L. Silva, V.A. Machado, Bernardo G. Almeida, J.P. Araújo, Maria-João R.P. Queiroz, Elisabete M.S. Castanheira, Paulo J.G. Coutinho, Solid and aqueous magnetoliposomes as nanocarriers for a new potential drug active against breast cancer, *Coll. Surf. B: Biointerfaces*, **2017**, 158, 460-468
- <sup>24</sup> A. Yusuf, A. Brophy, B. Gorey, A. Casey, Liposomal encapsulation of silver nanoparticles enhances cytotoxicity and causes induction of reactive oxygen species-independent apoptosis, *J. Appl. Toxicol.*, **2018**, 38, 616-627
- <sup>25</sup> J. Pichaandi, L. Tong, A. Bouzekri, Q. Yu, O. Ornatsky, V. Baranov, M. A. Winnik Liposome-Encapsulated NaLnF<sub>4</sub> Nanoparticles for Mass Cytometry: Evaluating Nonspecific Binding to Cells, *Chem. Mater.*, **2017**, 29, 4980–4990
- <sup>26</sup> Spray Drying Techniques for Food Ingredient Encapsulation, C. Anandharamakrishnan, Padma Ishwarya S. Eds., 2015, Wiley-Blackwell
- <sup>27</sup> C. J. Brinker, Y. Lu, A. Sellinger, H. Fan, Evaporation-Induced Self-Assembly: Nanostructures Made Easy, *Adv. Mater.*, **1999**, 11, 579-5885
- <sup>28</sup> G. M. Rotskoff, P. L. Geisslerb, Robust nonequilibrium pathways to microcompartment assembly, *Proc. Natl. Acad. Sci. U.S.A.*, **2018**, 115, 6341-6346
- <sup>29</sup> J. Lou, X. Zhang, M. D. Best, Lipid Switches: Stimuli-Responsive Liposomes through Conformational Isomerism Driven by Molecular Recognition. *Chem. - A Eur. J.*, **2019**, 25, 20–25
- <sup>30</sup> J. Lou, A. J. Carr, A. J. Watson, S. I. Mattern-Schain, M. D. Best, Calcium-Responsive Liposomes via a Synthetic Lipid Switch. *Chem. - A Eur. J.*, **2018**, 24, 3599–3607
- <sup>31</sup> S. Wilhelm, Perspectives for Upconverting Nanoparticles, *ACS Nano*, **2017**, 11, 10644–10653
- <sup>32</sup> S. A. Walker, M. T. Kennedy, J. A. Zasadzinski, Encapsulation of Bilayer Vesicles by Self-Assembly, *Nature*, **1997**, 387, 61–64
- <sup>33</sup> S. Simões, J. Nuno Moreira, C. Fonseca, N. Düzgünes, M. C. Pedroso de Lima, On the formulation of pH-sensitive liposomes with long circulation times, *Adv. Drug Deliv. Rev.*, **2004**, 56, 947–965
- <sup>34</sup> E. Fattal, P. Couvreur, C. Dubernet, “Smart” delivery of antisense oligonucleotides by anionic pH-sensitive liposomes, *Adv. Drug Deliv. Rev.*, **2004**, 56, 931–946
- <sup>35</sup> S. Mura, J. Nicolas, P. Couvreur, Stimuli-responsive nanocarriers for drug delivery, *Nature Mater.*, **2013**, 12, 991-1003
- <sup>36</sup> K. M. J. Saeuens, J. Zhang, I. N. A. Van Bogaert, W. Soetaert, Cloning and functional characterization of the UDP-glucosyltransferase UgtB1 involved in sophorolipid production by *Candida bombicola* and creation of a glucolipid-producing yeast strain, *Yeast*, **2011**, 28, 279-292
- <sup>37</sup> N. Baccile, A.-S. Cuvier, S. Prévost, C. V Stevens, E. Delbeke, J. Berton, W. Soetaert, I. N. A. Van Bogaert, S. Roelants, Self-Assembly Mechanism of pH-Responsive Glycolipids: Micelles, Fibers, Vesicles, and Bilayers, *Langmuir*, **2016**, 32, 10881–10894.
- <sup>38</sup> P. Dhasaiyan, B. L. V. Prasad, Self-Assembly of Bolaamphiphilic Molecules, *Chem. Rec.*, **2017**, 17, 597–610.
- <sup>39</sup> D. Kitamoto, T. Morita, T. Fukuoka, M. Konishi, T. Imura, Self-assembling properties of glycolipid

---

biosurfactants and their potential applications, *Curr. Op. Coll. Interf. Sci.*, **2009**, *14*, 315–328.

- <sup>40</sup> I. N. Van Bogaert, K. Saerens, C. De Muynck, D. Develter, W. Soetaert, E. J. Vandamme, Microbial production and application of sophorolipids, *Appl. Microbiol. Biotechnol.*, **2007**, *76*, 23–34
- <sup>41</sup> N. Baccile, F. Babonneau, I. M. Banat, K. Ciesielska, A.-S. Cuvier, B. Devreese, B. Everaert, H. Lydon, R. Marchant, C. A. Mitchell, S. Roelants, L. Six, E. Theeuwes, G. Tsatsos, G. E. Tsotsou, B. Vanlerberghe, I. N. A. Van Bogaert, W. Soetaert,, Development of a Cradle-to-Grave Approach for Acetylated Acidic Sophorolipid Biosurfactants, *ACS Sustain. Chem. Eng.*, **2017**, *5*, 1186–1198
- <sup>42</sup> E. I. P. Delbeke, J. Everaert, O. Lozach, T. Le Gall, M. Berchel, T. Montier, P.-A. Jaffrès, P. Rigole, T. Coenye, M. Brennich, N. Baccile, S. L. K. W. Roelants, W. Soetaert, I. N. A. Van Bogaert, K. M. Van Geem, C. V. Stevens, Synthesis and biological evaluation of bolaamphiphilic sophorolipids, *ACS Sustain. Chem. Eng.*, **2018**, *6*, 8992–9005
- <sup>43</sup> L. Van Renterghem, S. L.K.W. Roelants, N. Baccile, K. Uyttersprot, M. C. Taelman, B. Everaert, S. Mincke, S. Ledegen, S. Debrouwer, K. Scholtens, C. Stevens, W. Soetaert From lab to market: An integrated bioprocess design approach for new-to-nature biosurfactants produced by *Starmerella bombicola*, *Biotechnol. Bioeng.*, **2018**, *115*, 1195–1206
- <sup>44</sup> H. L. Lydon, N. Baccile, B. Callaghan, R. Marchant, C. A. Mitchell, I. M. Banat Adjuvant antibiotic activity of acidic sophorolipids with potential for facilitating wound healing, *Antimicrob. Agents Chemother.*, **2017**, *61*, e02547-16
- <sup>45</sup> Y. Hirata, M. Ryu, K. Igarashi, A. Nagatsuka, T. Furuta, S. Kanaya, M. Sugiura, Natural synergism of acid and lactone type mixed sophorolipids in interfacial activities and cytotoxicities, *J. Oleo Sci.* **2009**, *58*, 565–572
- <sup>46</sup> N. Baccile, M. Selmane, P. Le Griel, S. Prévost, J. Perez, C. V. Stevens, E. Delbeke, S. Zibek, M. Guenther, W. Soetaert, I. N. A. Van Bogaert, S. Roelants, pH-driven self-assembly of acidic microbial glycolipids, *Langmuir*, **2016**, *32*, 6343–6359
- <sup>47</sup> E. Johnson, D. Cascio, M. R. Sawaya, M. Gingery, I. Schröder, Crystal Structures of a Tetrahedral Open Pore Ferritin from the Hyperthermophilic Archaeon *Archaeoglobus fulgidus*, *Structure*, **2005**, *13*, 637–648
- <sup>48</sup> R. Massart, *IEEE Trans. Magn.*, **1981**, *17*, 1247
- <sup>49</sup> R. Massart, V. Cabuil, *J. Chim. Phys.*, **1987**, *84*, 7
- <sup>50</sup> C. Felip-León, F. Guzzetta, B. Julián-López, F. Galindo, J. F. Miravet, Multimodal Light-Harvesting Soft Hybrid Materials: Assisted Energy Transfer upon Thermally Reversible Gelation, *J. Phys. Chem. C*, **2017**, *121*, 39, 21154–21159
- <sup>51</sup> B. Sana, E. Johnson, S. Lim, The Unique Self-assembly/disassembly Property of *Archaeoglobus fulgidus* Ferritin and Its Implications on Molecular Release from the Protein Cage, *Biochim. Biophys. Acta – Gen. Sub.*, **2015**, *1805*, 2544–2551
- <sup>52</sup> A. Walter, P. K. Vinson, A. Kaplun, Y. Talmon, *Biophys. J.*, **1991**, *60*, 1315–1325.
- <sup>53</sup> L.-A. Tai, P.-J. Tsai, Y.-C. Wang, Y.-J. Wang, L.-W. Lo, C.-S. Yang, *Nanotechnology*, **2009**, *20*, 135101
- <sup>54</sup> C. A. Monnier, D. Demurtas, C. Jud, D. Vanhecke, *ACS Nano*, **2014**, *8*, 3451–3460
- <sup>55</sup> N. Baccile, R. Noiville, L. Stievano, Inge Van Bogaert, Sophorolipids-functionalized iron oxide nanoparticles, *Phys. Chem. Chem. Phys.*, **2013**, *15*, 1606
- <sup>56</sup> E. Amstad, T. Gillich, I. Bilecka, M. Textor and E. Reimhult, Ultrastable Iron Oxide Nanoparticle Colloidal Suspensions Using Dispersants with Catechol-Derived Anchor Groups, *Nano Lett.*, **2009**, *9*, 4042–4048



- 
- <sup>57</sup> E. Amstad, E. Reimhult, Nanoparticle actuated hollow drug delivery vehicles, *Nanomedicine* **2012**, 7, 145–164.
- <sup>58</sup> A. E., J. Kohlbrecher, E. Muller, T. Schweizer, M. Textor, E. Reimhult, Triggered Release from Liposomes through Magnetic Actuation of Iron Oxide Nanoparticle Containing Membranes, *Nano Lett.* **2011**, 11, 1664–1670
- <sup>59</sup> G. D. Bothun, M. R. Preiss, Bilayer heating in magnetite nanoparticle-liposome dispersions via fluorescence anisotropy, *J. Colloid Interface Sci.* **2011**, 357, 70–74
- <sup>60</sup> S. Nappini, M. Bonini, F. B. Bombelli, F. Pineider, C. Sangregorio, P. Baglioni, B. Nordèn, Controlled drug release under a low frequency magnetic field: Effect of the citrate coating on magnetoliposomes stability, *Soft Matter* **2011**, 7, 1025–1037

## Supporting Information

### Figure captions

Figure S 1 - TEM images of bare iron oxide NPs, NPs-SLs at pH 6 (NPs SL pH6, sample S5) and NPs- GLs at pH 9 (NPs GL pH9, sample S2). Solutions have been dried directly on the TEM grid before observation.

Figure S 2 - a) TEM images of NPs GL samples at pH 6 (sample S3). b-d) TEM images of sample S4 (NPs GL, pH 2  $\rightarrow$  pH 6). Solutions are dried on the TEM grid before observation. The Fourier Transform (FT) performed on the rectangle-highlighted region has been denoised (bottom left image c)) to better put in evidence the crystalline network in the inverse FT image (bottom right d)).

Figure S 3 - Cryo-TEM images of NPs GL samples at pH below 4 adjusted from pH 9

Figure S 4 – Cryo-TEM images of a NP-free GC18 :1 solution at 0.5 w% in water at the final pH 6, after treating the solution at pH 9  $\rightarrow$  pH 2  $\rightarrow$  pH 6, by adding few  $\mu$ L of 1M HCl and 0.1 M NaOH

Figure S 5 – Qualitative illustration of the encapsulation efficiencies for different batches. a) Control: GL vesicles in water at pH 6 next to a neodymium magnet; b) Typical image of a succesful encapsulation event with encapsulation efficiency lower than 50%. c) Typical image of a succesful encapsulation event with encapsulation efficiency higher than 50%.

Figure S 6 – a) XRD, b) TEM and c) size distribution (from TEM) of NaYF<sub>4</sub>:Yb/Ln (Ln= Er or Tm) nanoparticle samples used in this work. d) Typical XRD pattern of NaYF<sub>4</sub>:Yb/Er encapsulated in GL vesicles after *manual pH jump (approach 2)*. The sample has been freeze-dried before characterization. e) DTA profiles of NaYF<sub>4</sub>:Yb/Er, encapsulated (in GL) NaYF<sub>4</sub>:Yb/Er and free GL. All NaYF<sub>4</sub>:Yb/Ln samples are stabilized by an oleic acid coating.

## **Supporting Information**

### **Easy formation of functional liposomes in water using a pH-responsive microbial glycolipid: encapsulation of magnetic and up-converting nanoparticles**

**Dr. Lisa Van Renterghem,<sup>a</sup> Dr. Fabrizio Guzzetta,<sup>b</sup> Patrick Le Griel,<sup>c</sup> Mohamed Selmane,<sup>c</sup> Dr. Ghazi Ben Messaoud,<sup>c</sup> Tabitha Tan Su Teng,<sup>d</sup> Prof. Sierin Lim,<sup>d</sup> Prof. Wim Soetaert,<sup>a,e</sup> Dr. Sophie Roelants,<sup>a,e</sup> Dr. Beatriz Julián-López,<sup>b</sup> Dr. Niki Baccile<sup>c,\*</sup>**

a - InBio – Center for Industrial Biotechnology and Biocatalysis, Department of Biotechnology, Faculty of Bioscience Engineering, Ghent University

b - Institute of Advanced Materials (INAM), Universitat Jaume I, Avda. Sos Baynat s/n, 12071 Castellón, Spain

c - Sorbonne Universités, CNRS, Collège de France, Chimie de la Matière Condensée de Paris UMR 7574, 4, Place Jussieu, 75005 Paris, France

d - School of Chemical and Biomedical Engineering, Nanyang Technological University, 70 Nanyang Dr., Singapore 637457, Singapore

e - Bio Base Europe Pilot Plant, Rodenhuisekaai 1, 9042 Gent, Belgium

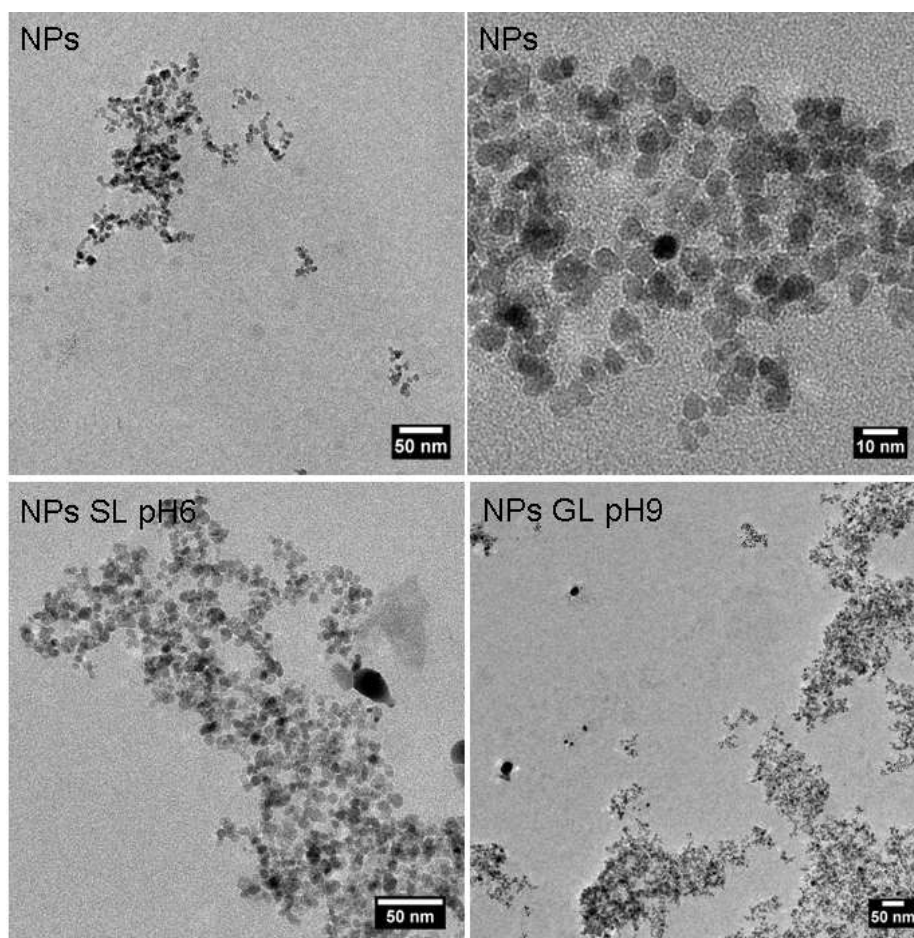


**Figure S 1 - TEM images of bare iron oxide NPs, NPs-SLs at pH 6 (NPs SL pH6, sample S5) and NPs- GLs at pH 9 (NPs GL pH9, sample S2). Solutions have been dried directly on the TEM grid before observation.**

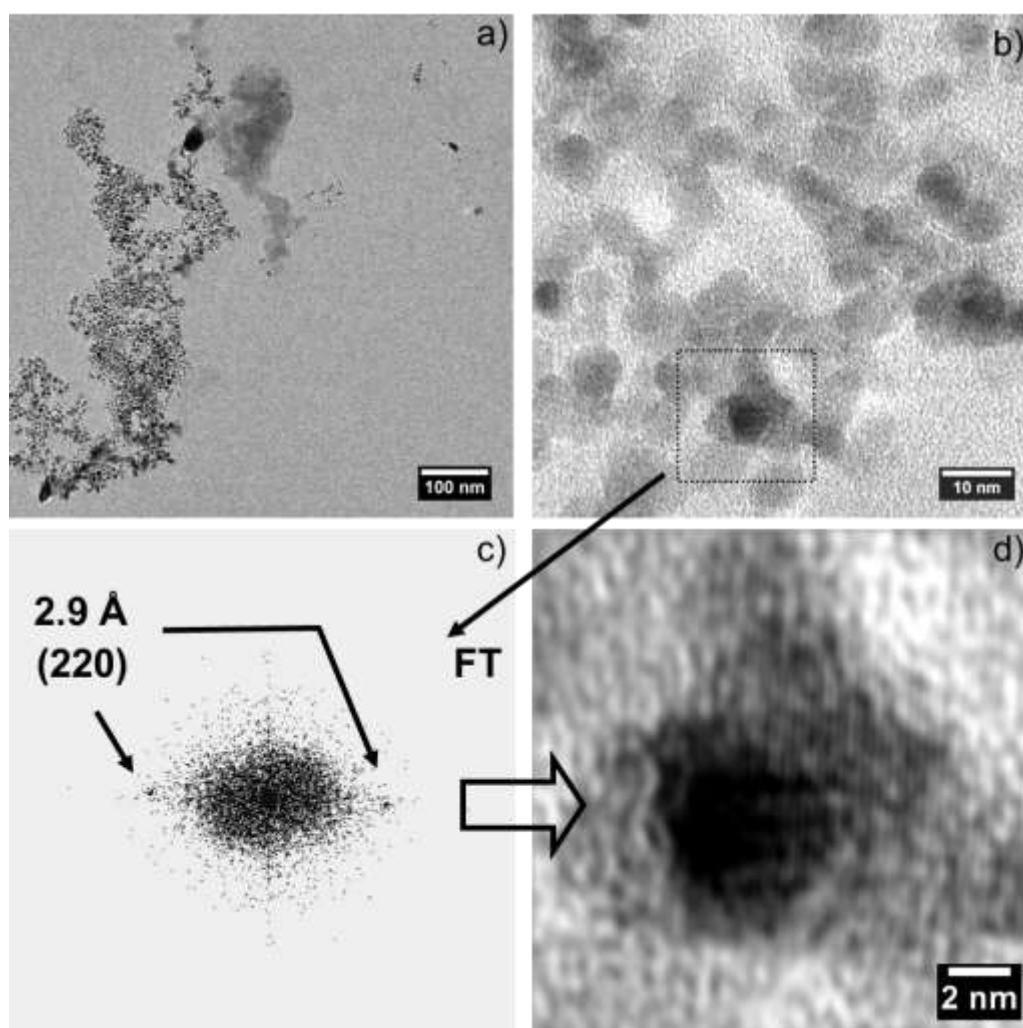


**Figure S 2 - a) TEM images of NPs GL samples at pH 6 (sample S3). b-d) TEM images of sample S4 (NPs GL, pH 2 → pH 6). Solutions are dried on the TEM grid before observation. The Fourier Transform (FT) performed on the rectangle-highlighted region has been denoised (bottom left image c)) to better put in evidence the crystalline network in the inverse FT image (bottom right d)).**

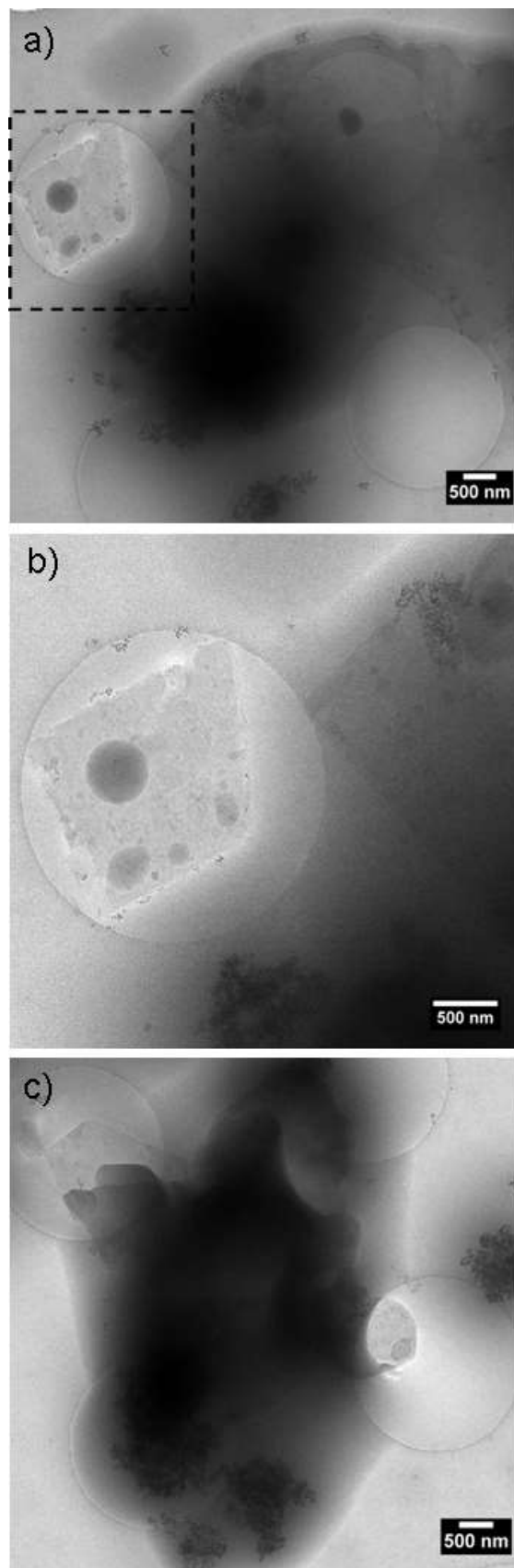


**Figure S 3 - Cryo-TEM images of NPs GL samples at pH below 4 adjusted from pH 9**

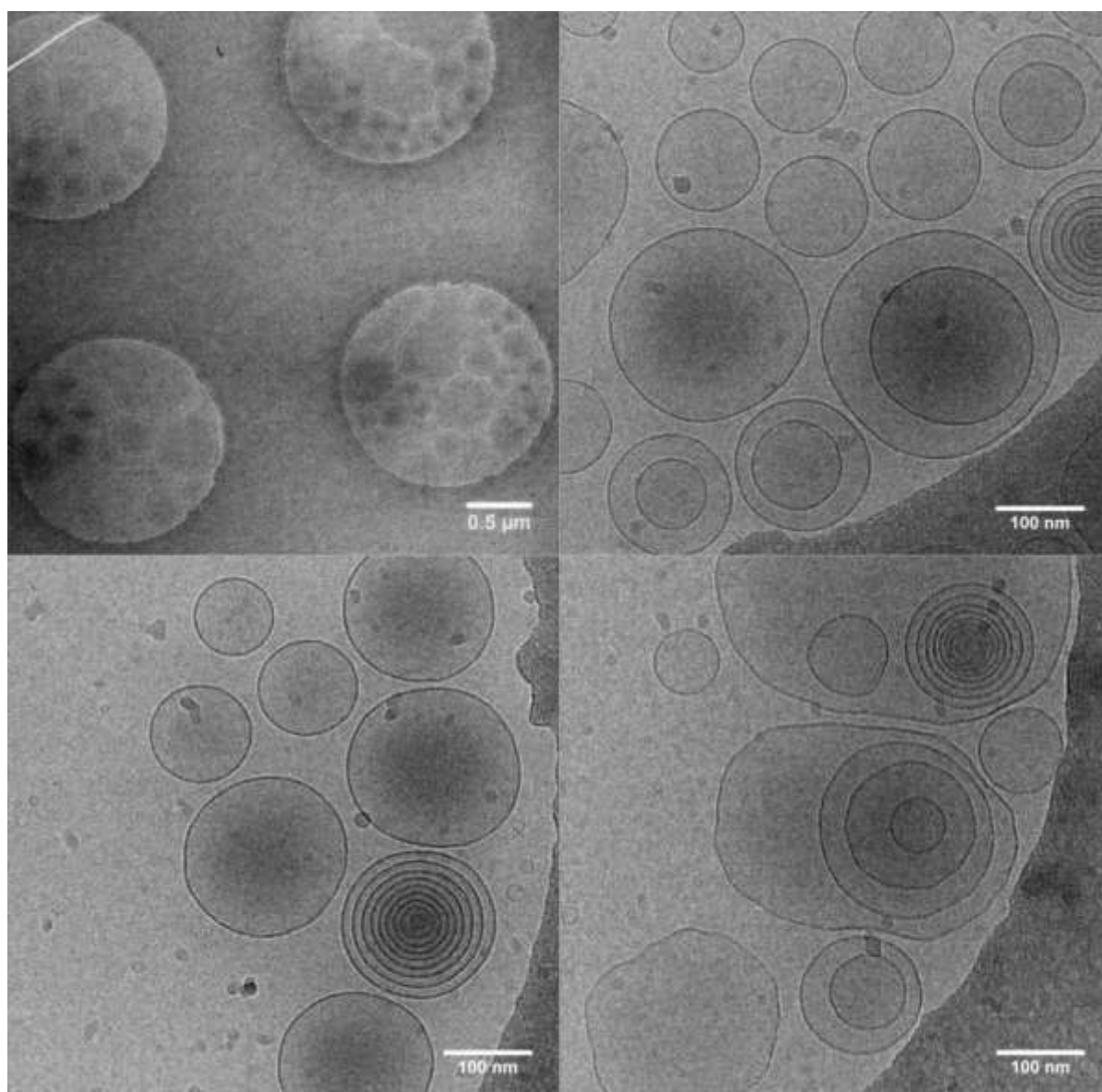


**Figure S 4 – Cryo-TEM images of a NP-free GC18 :1 solution at 0.5 w% in water at the final pH 6, after treating the solution at pH 9 → pH 2 → pH 6, by adding few μL of 1M HCl and 0.1 M NaOH**

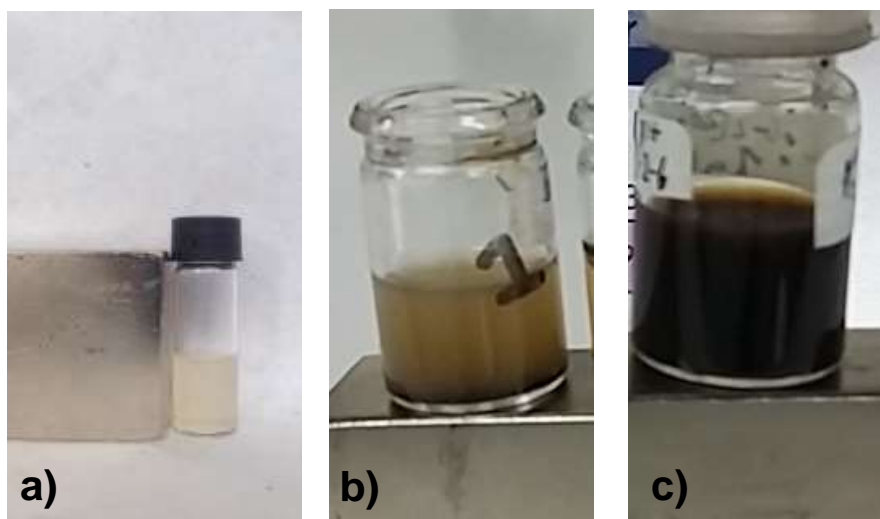


**Figure S 5 – Qualitative illustration of the encapsulation efficiencies for different batches. a) Control: GL vesicles in water at pH 6 next to a neodymium magnet; b) Typical image of a succesful encapsulation event with encapsulation efficiency lower than 50%. c) Typical image of a succesful encapsulation event with encapsulation efficiency higher than 50%.**



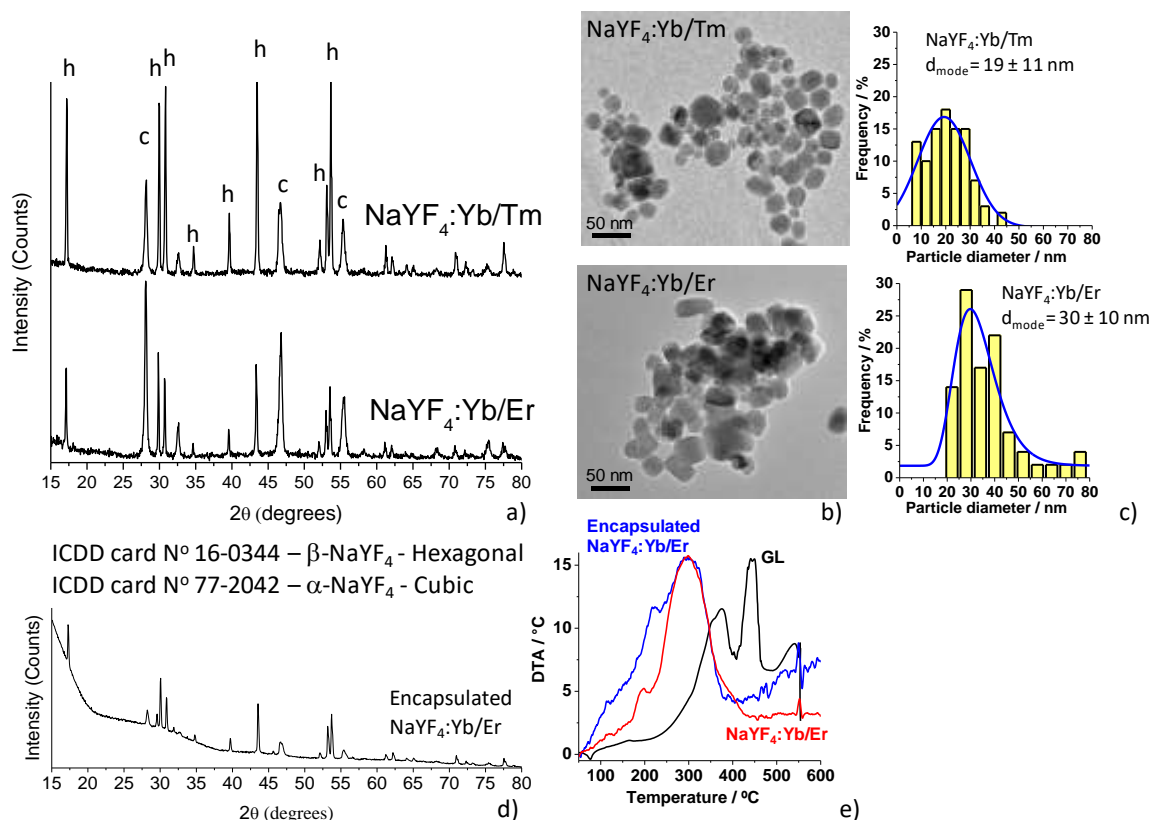


**Figure S 6 – a) XRD, b) TEM and c) size distribution (from TEM) of NaYF<sub>4</sub>:Yb/Ln (Ln= Er or Tm) nanoparticle samples used in this work. d) Typical XRD pattern of NaYF<sub>4</sub>:Yb/Er encapsulated in GL vesicles after *manual pH jump (approach 2)*. The sample has been freeze-dried before characterization. e) DTA profiles of NaYF<sub>4</sub>:Yb/Er, encapsulated (in GL) NaYF<sub>4</sub>:Yb/Er and free GL. All NaYF<sub>4</sub>:Yb/Ln samples are stabilized by an oleic acid coating.**